The diurnal cycle of the smoky marine boundary layer observed during August in the remote southeast Atlantic

Jianhao Zhang[1] and Paquita Zuidema[1]

[1]Rosenstiel School of Marine and Atmospheric Science, University of Miami, 4600 Rickenbacker Cswy, Miami, FL, 33149 USA

Correspondence: Jianhao Zhang (jzhang@miami.edu) and Paquita Zuidema (pzuidema@miami.edu)

Abstract.

Ascension Island (8° S, 14.5°W) is located at the northwestern edge of the south Atlantic stratocumulus deck, with most clouds in August characterized by surface observers as "stratocumulus and cumulus with bases at different levels", and secondarily as "cumulus of limited vertical extent" and occurring within typically decoupled boundary layer. Field measurements have previously shown that the highest amounts of sunlight-absorbing smoke occur annually within the marine boundary layer during August. On more smoke-free days, the diurnal cycle in cloudiness includes a nighttime maximum in cloud liquid water path and rain, an afternoon cloud minimum and a secondary late-afternoon increase in cumulus and rain. The afternoon low-cloud minimum is more pronounced on days with smokier boundary layer. The cloud liquid water paths are also reduced throughout most of the diurnal cycle when more smoke is present, with the difference from cleaner conditions most pronounced at night. Precipitation is infrequent. An exception is the mid-morning, when the boundary layer deepens and liquid water paths increase. The data support a view that a radiatively-enhanced decoupling persisting throughout the night is key to understanding the changes in the cloud diurnal cycle when the boundary layer is smokier. Under these conditions, the nighttime stratiform cloud layer does not always recouple to the sub-cloud layer, and the decoupling maintains more moisture within the sub-cloud layer. After the sun rises, enhanced shortwave absorption in a smokier boundary layer can drive a vertical ascent that momentarily couples the sub-cloud layer to the cloud layer, deepening the boundary layer and ventilating moisture throughout, a process that may also be aided by a shift to smaller droplets. After noon, shortwave absorption within smokier boundary layers again reduces the upper-level stratiform cloud and the sub-cloud relative humidity, discouraging further cumulus development and again strengthening a decoupling that lasts longer into the night. The novel diurnal mechanism provides a new challenge for cloud models to emulate. The lower free troposphere above cloud is more likely to be cooler, when boundary layer smoke is present, and lower free-tropospheric winds are stronger and more north-easterly, with both (meteorological) influences supporting further smoke entrainment into the boundary layer from above.

1 Introduction

Shortwave-absorbing aerosols above the southeast Atlantic overlay and mix in with one of the earth's largest stratocumulus decks from July through October. Many studies highlight the presence and radiative impact of absorbing aerosol in the free troposphere (Waquet et al., 2013; Peers et al., 2015; Das et al., 2017; Sayer et al., 2019; Peers et al., 2019; Deaconu et al., 2019), and indeed recent aircraft measurements confirm the biomass-burning aerosol (BBA) is primarily in the free troposphere during the month of September (LeBlanc et al., 2019; Cochrane et al., 2019; Shinozuka et al., 2019). The above-cloud aerosol shortwave absorption can warm the free troposphere, all else equal, strengthening the capping inversion and reducing entrainment (Johnson et al., 2004; Gordon et al., 2018; Herbert et al., 2019). This may explain why stratocumulus thickens in September-October (Wilcox, 2010), and cloud cover and top-of-atmosphere all-sky albedo increase when more smoke is present (Adebiyi et al., 2015; Wilcox, 2012), aided perhaps by changes in other cloud-controlling factors and aerosol indirect effects (Fuchs et al., 2018; Adebiyi and Zuidema, 2018).

The process by which the clouds adjust to the presence of the absorbing aerosols depends critically on the relative location of the aerosol to the low-cloud deck (Johnson et al., 2004; Koch and Del Genio, 2010; Gordon et al., 2018; Herbert et al., 2019). Aerosol-cloud microphysical interactions that reflect the presence of smoke in the boundary layer have also been observationally documented for the southeast Atlantic (Costantino and Bréon, 2013; Painemal et al., 2014; Grosvenor et al., 2018; Diamond et al., 2018) and modeled (Yamaguchi et al., 2015; Zhou et al., 2017; Lu et al., 2018). In 2016, the Department of Energy Atmospheric Radiation Measurement program deployed its Mobile Facility 1 (AMF1; Miller et al., 2016) to the windward side of Ascension Island as part of the Layered Atlantic Smoke Interactions with Clouds (LASIC) field campaign (Zuidema et al., 2015), becoming one of several new campaigns focused on understanding smoke-cloud interactions above the southeast Atlantic (Zuidema et al., 2016b). Ascension Island (8°S and 14.5°W) is midway within the South Atlantic basin, about 2500 kilometers to the west of continental Africa and underneath the main outflow region of the BBA plumes from continental African fires during June through October (Adebiyi et al., 2015). Early results indicated the frequent presence of biomass-burning aerosols near the surface, with seasonal maxima in black carbon mass concentrations occurring in August (Fig. 1 and Zuidema et al., 2018). Prior to 2016, only one research aircraft campaign had documented the presence of smoke in the boundary layer of the remote SE Atlantic (Haywood et al., 2003).

To date, no observational studies (that we are aware of) have documented how clouds adapt radiatively to the presence of smoke within the southeast Atlantic boundary layer. Studies focusing on the smoke-filled boundary layers of other marine regions have shown that a decrease in relative humidity from a raised temperature will encourage reductions in low-cloud cover (Hansen et al., 1997; Ackerman et al., 2000). Johnson et al. (2004) indicate that shortwave absorption within a smoke-containing cloud layer can decouple an initially well-mixed boundary layer. The Cloud, Aerosol, Radiative forcing, Dynamics EXperiment based in the northern Maldives, concluded that smoke-polluted conditions coincided with reduced turbulence, with reduced entrainment at the top of the sub-cloud layer resulting in a shallower mixed layer of enhanced humidity (Pistone et al., 2016; Wilcox et al., 2016).

The August maximum in the near-surface refractory black carbon (rBC) mass concentrations motivate this study's focus on that particular month. In August, the boundary layer black carbon loadings can remain elevated for over a week, indicating persistent meteorological conditions, punctuated by shorter time periods with low smoke loadings (Fig. 1). This contrasts with the more frequent variations in boundary layer smoke loadings occurring during June and July, while in September the boundary layer smoke loadings decrease dramatically, with more of the biomass burning aerosol residing above the boundary layer (e.g., Shinozuka et al., 2019). The focus on one month only reduces the convolution of faster cloud responses with larger-scale seasonal meteorological changes. August boundary layer aerosol concentrations are similar to those within the September free troposphere (Shinozuka et al., 2019), but the ability of aerosol particles to absorb sunlight is more pronounced, with single scattering albedos ranging from 0.78 to 0.83 (Zuidema et al., 2018), lower than documented for the September free troposphere (Pistone et al., 2019; Cochrane et al., 2019). The combination of high aerosol concentrations and low single-scattering-albedo indicate the potential for a clear cloud response to a robust radiative warming of the boundary layer in August.

This study primarily infers the cloud response through examining observed changes in cloud properties across the diurnal cycle as a function of the smoke loading. This takes advantage of the more numerous samples of the diurnal cycle, compared to of a particular weather or synoptic regime; that shortwave-absorption can only occur during the day, potentially aiding interpretation; and complements analysis of daytime-only aircraft campaigns datasets. A remaining concern, that a synoptic bias is embedded in the respective selection of time periods, is explicitly addressed in Section 2. The smoke loading vary similarly with time across the two August months (2016 and 2017; Fig. 1), justifying a combined analysis, with the caveat that the maximum smoke loadings in August, 2016 are approximately double those in August, 2017.

Prior studies of the diurnal cycle of marine boundary layer clouds have shown distinct diurnal cycles between stratocumulus and cumulus, with stratocumulus cloud cover attaining a broad-in-time nighttime maximum ending at dawn, attributed to accumulated nighttime radiative cooling (e.g., Rozendaal et al., 1995; Eastman and Warren, 2014; Painemal et al., 2015; Burleyson and Yuter, 2015; Chellappan et al., 2018). Surface-forced cumuli clouds, in contrast, produce smaller cloud fractions with a maximum in the late afternoon (Eastman and Warren, 2014) and a minimum at sunrise. Similar diurnal cycles have been observed within the planet's major subtropical stratocumulus decks at their seasonal maximum (e.g., Klein et al., 1995; Ciesielski et al., 2001). Downstream of the main stratocumulus deck, as is the case for Ascension Island, the daytime breakup of stratocumulus can become more pronounced, amplifying the diurnal cycle (Rozendaal et al., 1995; Burleyson and Yuter, 2015) and supporting a transition from stratocumulus to cumulus. Miller and Albrecht (1995) and Miller et al. (1998) further indicate that mesoscale organization occurring in the late afternoon/early evening can be important for overcoming the stability of the sub-cloud transition layer for marine boundary layer clouds at the Azores, further supported within (Rémillard et al., 2012). Little is known of how significant smoke loadings within the boundary layer affect the diurnal cycle in marine stratocumulus cloud, however.

Further campaign site information, an overview of the monthly-mean diurnal cycle and the two August months, and the analysis approach are described in Section 2. The diurnal cycle in cloud properties as a function of "more" and "less" smoky conditions is put forth in Section 3, with examples from two days highlighting the observed features. Synthesis explanations for the observed cloud diurnal cycle are provided in Section 4. A case is made for how smoke-filled boundary layers support

the further entrainment of free-tropospheric smoke in Section 5. A discussion and summary, including of the impact on the top-of-atmosphere all-sky albedo, constitutes Section 6, with some additional figures included within a Supplement.

2 Data, compositing approach and overview

The highest point on the volcanic island is the 859 m peak of Green Mountain, with the AMF1 site located on its windward flank at 340 m above sea level. Orographic lifting supports the development of shallow cumulus clouds at the lifting condensation level (LCL) above the site, evident within satellite imagery under suppressed conditions and in a comparison of the vertical distribution of ceilometer-detected cloud base heights at the AMF1 site and those at the airport located four km to away (Fig. 2). For this reason the diurnal cycle in low-cloud properties is evaluated using geostationary satellite retrievals capable of a larger-scale overview, and the available airport measurements. In contrast, satellite visible imagery does not indicate an obvious impact from the mountain peak on the deeper boundary layers associated with the larger precipitating systems. We assume the AMF1 precipitation measurements can represent those of a larger region (at 340 m altitude). The in-situ aerosol measurements benefit from the AMF1 site's windward location, away from local sources of aerosol. The surface is a hard-packed volcanic rock surface with a thin soil, and the site's elevation reduces the contribution from sea spray (no dedicated sea salt measurements are available). Persistent southeasterly boundary layer winds (see Zuidema et al., 2015, for wind roses) encourage aerosol measurements that are representative of the sub-cloud layer above the open ocean, confirmed by comparisons to measurements from the UK CLARIFY (Cloud Aerosol Radiation Interactions and Forcing - Year 2017) aircraft campaign, based on Ascension in August-September of 2017 (Jonathan Taylor, pers. comm.).

2.1 LASIC datasets

The radiosondes were launched at the airport, located near sea level. The LASIC radiosondes form the first measurements of the thermodynamic structure diurnal cycle at this location. One benefit for this study is that, in August of 2016, eight radiosondes were launched daily every three hours, an increase from the campaign-norm of four times daily at 0, 6, 12, and 18 UTC. The Vaisala RS-92 radiosondes yielded 357 successful profile measurements of the complete boundary layer for the two Augusts. Measurements within the first 100 m were clearly affected by island heating, perhaps from the building in which the radiosondes were kept, and the radiosonde data within 100 m of sea level are discarded from the analysis. The radiosondes were launched from the southwestern side of the island, and the radiosondes spend approximately eight minutes above the island before advecting away from it. Afternoon warming is consistently evident in the potential temperature measurements up to 200 m, at times higher, and composite means can suggest a convectively unstable afternoon boundary layer. This may indicate some remaining island heating influence on the radiosonde temperatures above 100 m. A comparison to CLARIFY aircraft data from its ascent profile during the afternoon of 17 August 2017 was inconclusive. To alleviate concerns that 200-400 m layer-mean potential temperature (θ) values may reflect an island heating influence as well as aerosol shortwave absorption, 400-600 m layer-mean θ averages are also shown. We note individual profiles almost always indicated a deeper statically stable afternoon boundary layer because of the presence of a stable sub-cloud transition layer.

The individual profiles were re-gridded to a common ten-meter vertical spacing from the surface to five km. The lifting condensation level is calculated using the temperature and relative humidity of an air parcel originating from 1000 hPa (see Appendix; picking a higher altitude does not affect the inferred diurnal cycle in LCL). The cloud-top inversion bases correspond to the maximum height of relative humidities greater than 75 %, and the inversion tops to the local maximum in the saturated equilibrium potential temperature, following Yin and Albrecht (2000). The depth of the inversion layer (top-base) is restricted to 500 meter. Visual inspections provided a sanity check on the corresponding inversion strength (the difference in potential temperature between the inversion base and top).

Cloud/precipitation frequency altitude distributions are derived from the Ka-band vertical-pointing cloud radar (KAZR) using a threshold of -35 dBZ for every 15 minutes. The KAZR has a sensitivity of -29 dBZ at 2 km at a gate spacing of 30 m. The KAZR reflectivities are biased high by 4-6 dB compared to the scanning K-band radar, more apparent at lower reflectivities (Brad Isom, pers. comm.). The scanning radar is the more accurate of the two radars, as it was calibrated regularly using a reflector; the offset is not accounted for here. The sensitivity and vertical resolution are enough to detect most clouds, but does miss some thin, non-precipitating clouds. Ceilometer data are invoked to improve detection of all clouds. Cloud base heights are reported by the ceilometers at both the AMF1 and airport sites, every 15 seconds. Only the lowest cloud bases are used.

Only the cloud liquid water path (LWP) retrievals from the microwave radiometers at the airport are used. The August 2016 (2017) LWPs are physically retrieved from the microwave radiometer profiler (two-channel microwave radiometer) using the standard ARM operational retrieval algorithm (Turner et al., 2007). Although technically an all-sky LWP, surface observers only reported the presence of middle- and high-altitude clouds 5% of the time (Fig. 3a), with the radiometers not responsive to ice particles. Surface precipitation measurements are obtained every minute from a disdrometer at the AMF1 site. A one-hour rain frequency is derived from the ratio of one-minute disdrometer samples with rain rates > zero to the number of total samples.

The boundary layer smoke loadings are inferred from the rBC mass concentrations derived from a single particle soot photometer (Fig. 1), corroborated by carbon monoxide (CO) concentrations. Smoke cloud condensation nuclei (CCN) concentrations are ascertained at 0.4% supersaturation from a dual-chamber CCN particle counter at the AMF1 site. Selected examples of vertical aerosol extinction profiles are derived from the 532 nm wavelength micropulse lidar (MPL) following Delgadillo et al. (2018). An explained variance exceeding 0.5 is required between the normalized relative backscatter signals to a calculated molecular scattering profile above any cloud layer, indicating that the lidar is able to penetrate the cloud layer. The lidar measurements are calibrated using a new overlap function derived after the LASIC campaign, producing reasonable agreement between newly-derived extinction profiles and those from a Raman lidar at the Southern Great Plains DOE site (Paytsar Muradyan, pers. comm.).

The LASIC datasets, their uncertainties if known, instrument source and comments are summarized in Table 1. Further detail on the radiosondes' quality control and selection is provided in the Appendix. All times are reported in local solar time (LST), which is approximately one hour earlier than the UTC time.

2.2 satellite and surface-based cloud datasets and reanalysis

Three different satellite cloud datasets are incorporated into this study, each with different strengths. The diurnal cycle in cloud fractions and effective cloud top heights are retrieved using the Visible Infrared Solar-Infrared Split Window Technique (VISST; Minnis et al., 2008) from radiances measured by the Spinning Enhanced Visible and Infrared Imager (SEVIRI) onboard the geostationary Meteosat10 satellite. The areal means correspond to a four by four degree domain latitudinally centered on Ascension but with a longitudinal center slightly to the island's east (6°S to 10°S and 15°W to 11°W), done to preferentially capture the clouds more representative of the island. The low-cloud fractions are estimated from the pixel-level products at three km resolution, as the ratio of liquid-water cloud + suspected liquid-water cloud pixels to the total retrieved pixels within an one-hour time period. Near-surface smoke is occasionally misclassified as cloud at high solar zenith angles (i.e. sunrise and sunset), resulting in apparent liquid-water clouds with effective heights lower than 500 m. These "super low clouds" are excluded from the analysis.

The top-of-atmosphere (TOA) all-sky albedos from the Clouds and the Earth's Radiant Energy System (CERES) one-degree Synoptic products (Minnis et al., 2011) are used to infer a net all-sky radiative effect. The Moderate Resolution Imaging Spectroradiometer (MODIS) provides higher-resolution visible imagery, and a longer-term context based on ten years of monthly level-3 1° gridded datasets (Platnick and coauthors, 2017). Both the monthly-mean MODIS and daily-mean CERES products, combined from both Terra and Aqua platforms, are areal-averaged over the same four by four degree domain as the SEVIRI data. In general, CERES retrievals of low-cloud fraction are slightly lower (by ~1.2% in August 2016 and ~3.2% in August 2017) than those from SEVIRI (Fig. 4). While the full causes are unknown, one contributing cause may be the twice-a-day sampling available to CERES versus the fully-resolved diurnal cycle available to SEVIRI. Surface observers from the United Kingdom's Meteorological Office at Ascension Island, trained to look away from the island, reported cloud types following the World Meteorological Organization protocol (WMO, 1974) every three hours. These are available coded into three-hourly SYNOP (surface synoptic reports) and provide a detailed visual clue into the prevailing cloud morphology, more than is typically documented. The European Centre for Medium-Range Weather Forecasts (ECMWF) fifth generation atmospheric reanalysis provide subsidence profiles, a cloud-controlling measure not available from observations, available every hour and gridded to 0.25° spatial resolution.

2.3 Compositing approach

The basic approach is to compare the diurnal cycle in low-cloud properties corresponding to "more" and "less" smoky conditions. The conditional compositing is based on daily-mean rBC mass concentrations exceeding 500 ng m^{-3} or remaining below 100 ng m^{-3}. These values are approximately based on the tercile values from the August distributions of one-minute rBC mass concentration (Fig. 5), with a rounding off applied for ease of the readership. Days experiencing a change in air masses are also removed from the analysis, by constraining the standard deviations to within 50 and 120 ng m^{-3} for "less" and "more" smoky days, respectively. The overall selection yields two groups of the same size: 13 "more" smoky days (August 10, 11, 13, 14, 15,

30 and 31 from 2016 and August 11, 12, 14, 15, 16 and 19 from 2017), and 13 "less" smoky days (August 1, 2, 3, 24, 25 and 26 from 2016 and August 3, 5, 21, 22, 23, 24 and 25 from 2017).

The "less" smoky days will still contain some smoke in the boundary layer. Pennypacker et al. (2019) document that low-aerosol days at Ascension are dominated by precipitation scavenging, similar to the Azores (Wood et al., 2017). Their analysis, which includes twelve days from August, 2016, indicates the "less" smoky days can capture the dominant features of the low-aerosol cloud diurnal cycle. A concern remains whether other cloud-controlling factors differ between the two groups of days. They do; this is addressed further in Sections 5 and 6.

2.4 Monthly-mean overview of conditions at Ascension

The daytime ten-year August-mean cloud cover varies from 54% (mid-morning) to 42% (mid-afternoon), with August of 2016 (2017) being slightly more (less) cloudy than the ten-year means (Fig. S1). In contrast to the suppressed polluted shallow marine cumuli over the Indian ocean examined within Ackerman et al. (2000), Pistone et al. (2016), and Wilcox et al. (2016), the low clouds at Ascension Island occupy a deeper boundary layer, with the mean trade-wind inversion base located at approximately 1.6 km in August (Fig. S2 black box-whiskers). The clouds often occupy two layers, one with cumuli bases rooted at the lifting condensation level at ~700 m, and the other a stratiform layer occurring underneath the trade-wind inversion base (Fig. 2). The monthly-mean profiles indicate a stratification in the water vapor mixing ratio profiles that imply a decoupling coinciding with the sub-cloud transition layer (Fig. S2 b and e).

The most frequently-occurring surface-observed cloud type is "stratocumulus and cumulus with bases at different levels" (C_L=8, Fig. 3a), also called cumulus-under-stratocumulus (e.g., Miller et al., 1998). This cloud type occurs 77% of the time overall and is most frequent at 9 LST, when it occurs 90% of the time. The second most commonly-occurring cloud type is "cumulus of little vertical extent" (C_L=1). This occurs 16% of the time, most frequently just before midnight (approximately 32% of the time between 21-24 LST; Fig. 3b). Shallow cumulus by itself becomes less frequent after midnight with the appearance of the more two-layered cloud system (C_L=8). After sunrise, the two-layered cloud systems gradually become less frequent and more shallow cumulus occurring by itself is reported. More weak daytime surface-driven cloud growth can be supported by a weakly-warming ocean surface, with buoy sea surface temperature measurements at 10°S, 10°W indicating a slight afternoon rise (~0.05 K) in quiescent conditions (not shown). Stratocumulus (C_L=5) is infrequent and mostly occurs just before sunrise if so.

Compared to locations that are closer to and poleward of the large subtropical stratocumulus decks, C_L=8 and C_L=1 are more common and C_L=5 is more occasional at Ascension (Klein et al., 1995; Painemal et al., 2010). A greater prevalence of surface-driven cumulus is consistent with Ascension's equatorward location and the overall warmer sea surface temperatures of the southeast Atlantic (Zuidema et al., 2016a) compared to the southeast Pacific. The diurnal cycle in C_L=8 also differs with location. Painemal et al. (2010) associate C_L=8 with large closed cells and a nighttime cloud fraction maximum slightly upwind of the eastern edge of main southeast Pacific stratocumulus deck, while Klein et al. (1995) report a mid-afternoon frequency maximum in C_L=8 at the poleward western edge of the northeast Pacific stratocumulus deck.

2.5 August time series

Two pronounced multi-day smoke events are apparent during each of the two months (Fig. 4), with the ones during mid-August lasting slightly longer than the ones at the end of the month. The 12-16 August 2016 period is the smokiest of the entire campaign, with rBC mass concentration reaching 1700 ng m^{-3}, analyzed further in Zuidema et al. (2018). Cleaner episodes occur at the beginning of the month and in-between the smokier events. Only during 21-23 August, 2017 do the rBC mass concentrations effectively approach zero continuously for about three days, and the CO concentrations decrease to the background level of 50-60 ppb representative of the pristine southern oceans (Allen et al., 2011; Shank et al., 2012).

The daily areal-mean low-cloud fraction tends to reduce during the smokier time periods, most clearly evident during mid-August, 2016 (Fig. 4, upper panel), and precipitation is less frequent and less intense during smokier time periods (Fig. 4, green line). The time series suggests that the reduction in low-cloud cover coincides with more "cumulus of little vertical extent" during the smokier conditions, documented further in Section 3. An exception occurs on 30-31 August, 2016, when smokier conditions in the boundary layer coincide with overcast stratocumulus. This time period indicates how quickly the seasonal transition can occur. The large-scale conditions began to resemble those for September, with a stronger subsidence at 800 hPa, stronger cloud top inversions, and stronger winds in the free troposphere (not shown). The first ORACLES-2016 (ObseRvations of Aerosols above CLouds and their intEractionS - Year 2016) flight occurred on 31 August, 2016, to the east-southeast of Ascension, and sampled the most polluted boundary layer of the September campaign, with Diamond et al. (2018) documenting overlying smoke in contact with the stratocumulus deck for several days. After 31 August, 2016, the boundary layer became much cleaner, both within the ORACLES flights and at Ascension, (Fig. 1 and Shinozuka et al., 2019). Although not explored further here, the change in the large-scale conditions is consistent with a seasonal evolution to stronger higher-altitude free-tropospheric winds (Adebiyi and Zuidema, 2016) that is more able to keep more of the smoke plume well above the boundary layer.

3 The low-cloud diurnal cycle as a function of the smoke loading

The diurnal cycle in the domain-averaged SEVIRI low-cloud fraction indicates a broad nighttime maximum peaking near or slightly after sunrise, after a mid-afternoon minimum extending to sunset (Fig. 6). In both years the low-cloud fraction is less during all hours of the day for the smokier time periods, with a more pronounced late-afternoon cloud reduction in August, 2016. The diurnal-mean cloud fractions in 2016 (2017) of 68% (57%) under "less" smoky conditions reduce to 45% (40%) when smoke loadings are higher in the boundary layer. The diurnal variation in 2016 is greater under smokier conditions, increasing from 17% to 48%, whereas it remains similar in 2017 regardless of smoke loading (35%).

The changes in the diurnal cycle of the cloud liquid water paths (LWPs; Fig. 7 a and b, based on three-hourly averages of one-minute LWP > 0 values only) do not fully conform to that in the areal-average cloud cover. The two years are shown separately as their diurnal cycles are slightly different (note differences in their range of values). For the "less" smoky days, there is a nighttime LWP maximum that corresponds with maxima in the nighttime rain frequencies and rates (Fig. 7 c and d). The cloud condensation nuclei concentrations (CCN) at 0.4% supersaturation have daily-mean values of 114 cm^{-3} for the less

smoky conditions, and the higher LWPs can produce rain capable of cleansing the aerosol loading further (e.g., Pennypacker et al., 2019). In both years, the median LWPs are less during much of the diurnal cycle when the boundary layer is smokier. The decrease is particularly noticeable at night. A nighttime maximum in rain frequency is still apparent, with a secondary late afternoon maximum, but rain occurs less frequently and the rain rates tend to be less under smokier conditions. More interestingly, in both years the LWPs tend to increase after sunrise during the smokier days. The post-sunrise increase in LWP is not accompanied with an overall increase in rain frequency or intensity, however. This suggests that the smoke aerosol can also suppress rain, consistent with daily-mean CCN concentrations at 0.4% supersaturation of 790 cm^{-3} for the smokier conditions.

Vertically-resolved cloud frequencies derived from the Ka-band zenith pointing cloud radar, aggregated every six hours, indicate fewer clouds at almost all altitudes, at all times of day, when the boundary layer is smokier (Fig. 8). The radar-perceived cloud bases tend to be higher, and the cloud tops lower. The two separate cloud layers are arguably more apparent under heavier smoke loadings. Higher cloud tops are more frequent in the morning (06 – 12 LST) under smokier conditions - consistent with higher upper quartiles of LWP between 08 – 10 LST (Fig. 7). Satellite measurements confirm that cloud top heights are typically lower under smokier conditions (Fig. 9). Cloud top heights in a smokier boundary layer are approximately one km at the lowest cloud fractions, indicating that the upper stratiform cloud layer is likely not present. The exception is in the morning just after sunrise. Almost all 08 LST samples (Fig. 9, green crosses), regardless of smoke loading, have a cloud effective height above 1.5 km, consistent with the radar observations (Fig. 8).

Surface observer reports are consistent with less stratiform cloud under smokier conditions, with more reports of "cumulus with little vertical extent", and less "stratocumulus and cumulus with bases at different level" (Fig. 10). The latter decreases from 83% to 67% in a smokier boundary layer, whereas the occurrence of "cumulus with little vertical extent" increases from 12% to 31% when the boundary layer is smokier. The shift between the two cloud types is most pronounced from midnight until 9 LST (not shown), suggesting the upper-level stratiform layer has more trouble reforming at night under smokier conditions.

Two days, chosen because MODIS satellite visible imagery are available for both overpasses (Fig. 11), also depict meaningful features that may otherwise be averaged over within composite means. One day, 12 August, 2017, is included in the "more" smoky composite (daily-mean rBC of 663 ng m^{-3}), while the smoke loading on 20 August, 2017, was intermediate at 346 ng m^{-3}. More developed cumuli clouds reaching and detraining near the inversion base occur near or after sunrise on both days, with precipitation reaching the surface. Thin stratiform layers, at times detected by the ceilometer but not by the cloud radar, primarily appear associated with detrainment from cumulus in the satellite imagery, although can also be detached. By the mid-afternoon, the stratiform cloud has thinned further or dissipated completely, with scattered cumuliform clouds dominating the radar and satellite imagery. The clouds are primarily cumuliform during the night. More precipitation reaches the ground on August 20, consistent with a deeper boundary layer. In both cases, the cloud base rises during the day, with more shallow cumuli reappearing after 1400 LST and recurring throughout the night.

The radiosonde profiles from both days indicate a boundary layer deepening accompanying the mid-morning cumuli cloud development (Fig. 12). On 12 August, 2017 the boundary layer deepens from approximately 1350 m at 5 LST to 1700 m at 11 LST, collapsing back to a depth of approximately 1300 m after 17 LST (Fig. 12a). The water vapor mixing ratio (q_v) profiles

suggest that the boundary layer is decoupled all day, but the moisture stratification is more clear at night; the q_v profiles at 5 LST on 12 August and 23 LST on 20 August indicate a q_v decrease with height of ~ 2 g kg^{-1} at $\sim$700 m. By 11 LST, some of the sub-cloud moisture appears to have ventilated upwards on both days. Also notable is the rising daytime cloud base (Fig. 11a), consistent with a clear reduction in the sub-cloud relative humidity (RH, Fig. 12a).

4 Explanations for the cloud diurnal cycle

When Figs. 6 – 12 are viewed in their totality, a picture emerges in which shortwave absorption reduces the rh below 100%, reducing daytime low-cloud amount more substantially under smokier conditions (Ackerman et al., 2000). The enhanced shortwave absorption can also strnegthen the daytime decoupling (e.g., Johnson et al., 2004). Of more interest, because it is a new observation, is the nighttime reduction in cloud cover and LWP under smokier conditions, corresponding to surface reports of less stratiform cloud but more shallow cumulus. This can either reflect an inability of longwave radiative cooling to reestablish a stratiform cloud layer, or, should the stratiform layer be present, to generate enough turbulence to reconnect the upper cloud layer with the surface. Instead, intermittent cumulus coupling can explain the occasional rain and higher liquid water paths, and can also take place after sunrise.

We examine the thermodynamic profiles to see if they are consistent with these ideas. The individual profiles of θ, rh, q_v and equivalent potential temperature (θ_e) are highly variable (Fig. 13). Individual trade-wind inversion heights vary from 1.5 to 2.2 km and are sharper than that within the mean profile. The sub-cloud layer is both warmer and moister than that of the ARM Eastern Northern Atlantic (ENA) site at the Azores (Rémillard et al., 2012). The sub-cloud layer is typically well-mixed, with a mean θ of $\sim$296 K and mean q_v of $\sim$13 g kg^{-1}. The sub-cloud layer is slightly cooler, by $\sim$3 K, and moister, by 1-3 g kg^{-1}, than the cloud layer above, with the two layers often distinctly separated through a transition layer somewhere between 500-700 m. Overall these indicate a boundary layer that is typically statically stable, primarily because of the sub-cloud transition layer. This discourages upward mixing, while the moisture within the sub-cloud layer increases its moist static energy and supports an conditional instability in which sub-cloud layer air, once lifted to the cloud layer, will readily mix further upwards to the trade-wind inversion, condensing en route.

Both the individual and mean profiles indicate that the mean boundary layer is deeper, by approximately 200 meters, when the smoke loading is higher (Fig. 13). The deepening is more defined in August 2016 than in August 2017, but the occurrence in both years suggests a common physical cause as opposed to a sampling bias. The deepening of the smokier boundary layers is most clearly evident at 8 LST, after a nighttime boundary layer shoaling (Fig. 14a). At 8 LST, under smokier conditions, the lower km is more well-mixed in temperature and moisture up to 600-700 m, and warmer and more moist up into the cloud layer, with higher relative humidities that are able to support more cloud cover (Fig. 14b-d).

The 200-400 m layer-mean θ warms in the afternoon by ~ 0.5 K regardless of the smoke loading, with the cooling mostly occurring just after sunset. The layer is overall $\sim$0.5 K warmer under smokier conditions (Fig. 15), indicating that the radiative warming does not dissipate away at night. The diurnal cycle in the 400-600 m layer-mean θ is similar, although muted, with a noontime static instability relative to the lower layer that may reflect island heating.

The 200-400 m layer q_v initially increases in the late afternoon/early evening irrespective of the smoke loading, consistent with the afternoon decoupling and preceding the late-night peaks in rain frequency (Fig. 7c). When more smoke is present, the accumulation of q_v continues into the early morning, and the post-midnight 200-400 m layer becomes more moist, by 0.25-0.5 g kg^{-1}, compared to that under "less" smoky conditions (Fig. 15b). During the early morning, the q_v decreases regardless of the smoke loading, consistent with an upward ventilation of moisture, and reaching its daily minimum after sunrise. A few individual "less" smoky soundings reflect near-surface rain evaporation through creation of a cold pool (Fig. 13a).

The diurnal cycle in the sub-cloud rh (Fig. 15c) reflects characteristics of both the temperature and q_v diurnal cycles, with a shift in the diurnal minimum from midday to mid-afternoon as the smoke loading increases. Consistent with changes in the relative humidities, the LCL rises during the day, reaching a maximum height of 700-800 m around 14 – 16 LST, then decreasing around sunset and leveling off before midnight (Fig. 15d). Hignett (1991) connect the higher mid-afternoon LCL to a suppression in turbulence independent of absorbing aerosol, but the cloud bases are higher when more smoke is present, serving as an independent confirmation of the decrease in sub-cloud rh. After midnight, under less smoky conditions, the cloud bases are above 900 m, exceeding the LCL by ∼200 m. This would be more indicative of an upper-layer stratiform layer reforming through longwave radiative cooling.

In the mid-morning, the difference between the LCL and cloud base heights decrease, more so under heavier smoke loadings, at the same time that the upper quartile LWP values indicate more vertical cloud development when the boundary layer is smokier (Fig. 7a and b) and deeper (Fig. 14). Given that rain remains infrequent (the examples in Fig. 11 notwithstanding), with low rain rates, there may also be a microphysical contribution to the morning deepening of the boundary layer. Non-precipitating shallow convection deepen more than do precipitating clouds in equilibrium conditions (Stevens, 2007; Stevens and Seifert, 2008), with the evaporation of small droplets above the base of the trade-wind inversion from overshooting cumulus turrets pre-conditioning the environment for further cloud development.

5   On the further entrainment of free-tropospheric smoke

More work is needed to fully ascertain how the black carbon detected within the boundary layer at Ascension arrived there. Given the presence of consistent southeasterly winds, most of the aerosol must have entered the boundary layer to the southeast of the island. One pathway is through entrainment from the free troposphere above, as a westward isentropic flow off of the African plateau located ∼1000 meters above sea level will place much of the biomass burning aerosols outflow above the low-cloud deck (e.g., Garstang et al., 1996). At Ascension in August, variability in the column aerosol optical depth is dominated by the variability in aerosol within the boundary layer (Zuidema et al., 2018). Nevertheless, a comprehensive visual inspection of the one-minute micropulse lidar extinction and depolarization profiles discerned that smoke was present above the island's boundary layer on every day the lidar was able to profile the free troposphere (20/23 days in August 2016/2017), multiply-layered at times up to five km. This indicates that the entrainment of smoke was likely ongoing for at least some of the days, although details of the vertical extinction profiles are uncertain enough that the detection of aerosol within the critical 100 m

above cloud top by the lidar is unreliable. Instead, we examine how the strength of the temperature inversion above cloud top varies with the boundary layer smoke loading, to ascertain how this may influence further entrainment.

Under lighter smoke loadings, increases in the smoke near the surface are associated with a stronger inversion (Fig. 16, correlation coefficient r of 0.3). In contrast, under higher smoke loadings, the inversion strength decreases significantly, from approximately 7 K to almost 4 K (r = -0.5), with further increases in smoke. The reduced inversion strength exceeds the reduction expected from a warming boundary layer alone (of 0.5 K, based on Fig. 15a). The relationship is also evident when only the time periods that coincide with the UK CLARIFY aircraft flights are evaluated (Fig. 16 dashed curves and asterisks).

The reduction in the inversion strength must therefore occur because of cooler θ profiles just above the cloud top. This is shown to occur during 14-15 August, 2016, when the highest boundary layer smoke loading of the two Augusts also coincided with the presence of some free-tropospheric smoke (Zuidema et al., 2018). Updated profiles of the temperature and aerosol extinction (Fig. S3) indicate an above-cloud θ of ~ 307 K, well below the mean value of ~ 310 K (Fig. 13). This is only one case, with attenuation of the lidar signal limiting a larger analysis, but does suggest that the horizontal advection that transports the aerosol to Ascension can also advect cooler continentally-influenced temperatures that have not yet warmed substantially through subsidence.

During 14-15 August, 2016, the winds at 800 hPa were more easterly than in the mean (Zuidema et al., 2018). A more comprehensive assessment of the winds, shown separately for the two years as a function of smoke loading (Fig. 17), indicates that at 2 km, just above the inversion top, times with stronger north-easterly winds become more frequent when the boundary layer is smokier (Fig. 17). These would facilitate a more efficient transport of smoke (when present) off of the continent, with the stronger winds and a more easterly momentum flux also encouraging the presence of more smoke within the boundary layer of the larger stratocumulus deck. Winds that are stronger in the boundary layer and lower free troposphere when the smoke loading is high is also consistent with the more "spun-up" circulation ascertained from reanalysis in Adebiyi et al. (2015). The mean wind speeds and wind roses also indicate that, regardless of smoke loading, the winds are the strongest from 200 m to 700 m, with a mean speed of approximately nine m s^{-1} and a consistent east-south-easterly direction, then decrease within the cloud layer and veer more to the east at higher altitudes.

We cannot discern a change in the inversion strength that can be related to aerosol above the cloud top (a free-tropospheric semi-direct effect), because of the limits to the lidar's above-cloud aerosol characterization. The August 1-10, 2016 case examined in the modeling study of Gordon et al. (2018), concluded that the intrusion of a significant smoke plume near Ascension ultimately strengthened the cloud deck, compared to a simulation without the smoke aerosol. One reconciliation with our observational results may be that older free-tropospheric aerosol layers continue to warm, explaining the presence of stronger inversions with increases of boundary layer smoke under more pristine conditions. It may be primarily more newly-advected free tropospheric aerosol that coexists with cooler potential temperatures, but the exploration of this idea is beyond the scope of this current study.

6 Discussion

The "typical" diurnal cycle for stratocumulus clouds is characterized by nighttime longwave radiative cooling of the stratiform cloud helping to couple the cloud to its surface moisture source, producing a nighttime maximum in LWP and precipitation. The two-cloud-layer "stratocumulus and cumulus with bases at different levels" (C_L=8), also known as stratocumulus-above-cumulus, is the most common cloud type at Ascension. It is most frequent in the morning after sunrise, when satellite visible imagery indicates these are large cumulus clusters, with individual cells easily spanning ∼40 km (e.g., Fig. 11). When more smoke is present, the cloud types reported by surface observers shift towards more "cumulus with little vertical extent" (C_L=1). Precipitation frequency and intensity are less when more smoke is present, although their diurnal phasing is not markedly altered. The liquid water path is less throughout most of the day, but most clearly so at night. The only time of day that is the exception occurs in the mid-morning, when LWPs can increase but rain frequency and intensity do not, in the mean.

We hypothesize that a radiatively-enhanced decoupling is the key to understanding the altered diurnal cycle. The boundary layer is typically decoupled regardless of the smoke loading, but becomes more so with more absorbing aerosol. The reduction in the daytime cloud cover with more smoke is easy to explain through increased shortwave absorption helping to decouple the cloud layer from the sub-cloud layer (e.g., Johnson et al., 2004). The afternoon cloud reduction is most evident in less upper-level stratiform layer, but a reduced sub-cloud relative humidity also inhibits cumulus cloud growth. After sunset, the cloud liquid water paths remain low, and the near-surface air is more moist than under lower smoke loadings. This supports the view that the late-afternoon decoupling is more likely to persist into and through the night, when more smoke is present.

As articulated in Miller et al. (1998), a stable sub-cloud transition layer can help support more vigorous open-cell convection, by encouraging the moisture stratification that provides the necessary convective available potential energy. In the Azores, this release of energy is primarily in the late afternoon and early evening, when the interface is the most stable. The sub-cloud layer is warmer and more moist at Ascension than at the ENA site in the Azores (Rémillard et al., 2012), and even more so when smoke is present in the boundary layer. The sub-cloud moisture increases the sub-cloud moist static energy throughout the night, with the moisture transported upwards after sunrise, when cloud liquid water paths increase within a deepening boundary layer.

Why is cumulus-coupling most likely to occur after sunrise, rather than late in the afternoon or during the night under smokier conditions? One explanation may be a radiatively-driven ascent that is more effective when the sub-cloud layer is better-mixed. The shortwave absorption (Q) can drive a vertical ascent (ω) through $\omega = \frac{Q}{\sigma}$, where σ is the static stability. The θ lapse rate within the 200–600 m layer is 0.835 K km^{-1} at 8 LST under smokier conditions, compared to 1.37 K km^{-1} for the less smoky composite. A radiative heating of the sub-cloud layer of one K day^{-1} can support a vertical ascent of 50 m hour^{-1}, which would suggest that four hours are required for the boundary layer to deepen by 200 m, longer than is observed. An additional heating may originate with the condensation of the upwardly-ventilated moisture. The liquid water paths increase, although no increase in the rain frequency is noted. Suppression of precipitation from the increased CCN concentrations may aid more evaporation of the smaller drops near and above the inversion base (Stevens, 2007; Stevens and Seifert, 2008), further

aiding the boundary layer deepening. The deepening supports entrainment that helps dissipate the upper-level cloud thereafter, aiding the subsequent reduction in cloud cover and cloud top heights (Fig. 9).

How does the diurnal cycle convolve with the stratocumulus-to-cumulus transition? Evidence of two separate processes appear within our analysis. Statistically, the shift away from cumulus-under-stratocumulus to more cumulus, when the boundary layer is smokier, is consistent with a transition that has started earlier (further upwind). More entrainment supported by the boundary layer morning deepening will hasten the transition, similar to the accelerated entrainment attributed to increased cloud droplet number concentrations within Zhou et al. (2017), but attributed primarily to shortwave absorption in this study. Aerosol-induced rain suppression, the cause for a delayed transition within Yamaguchi et al. (2015), could be active on 30-31 August, 2016, the only days within the two Augusts in which the main stratocumulus deck reached Ascension. Smoke entrained far upstream (Diamond et al., 2018) supplied CCN concentrations of $\sim$800 cm^{-3} at 0.4% supersaturation at Ascension. Although still a decoupled boundary layer, cumulus coupling in the mid-morning of 31 August strengthened a stratiform cloud that lasted through the day, with the SEVIRI-derived cloud droplet number concentration approaching 250 cm^{-3}. A more confident attribution for this case will also need to take September-like large-scale conditions into account.

The smoky episodes last longer during August than during June or July (Fig. 1). We hypothesize a positive feedback may contribute to the longevity of the week-long August smoke events. On smokier days, morning boundary layers are deeper and the cloud tops are higher. Stronger winds at the inversion top (Fig. 17c and g) will favor turbulent mixing across the inversion. Meanwhile, north-easterlies at 800 hPa are more frequent (Fig. 17 d and h), favoring lower-level transport of smoke off of the African continent that will reside closer to the stratocumulus cloud tops. The fresher aerosol can be transported within layers with cooler, more continentally-influenced, potential temperatures compared to the monthly-mean, and the cloud-top inversion strength decreases as a result (Fig. 16); boundary layer warming from shortwave absorption is not sufficient to produce a $\sim$3 K decrease in the inversion strength (Fig. 15). A weaker inversion favors aerosol entrainment into the boundary layer if smoke is present overhead. If so, the increased cloud droplet number concentrations will further aid entrainment through slowing cloud droplet sedimentation, while precipitation suppression (Fig. 4 and Fig. 7) can help conserve the boundary layer aerosol loading, by reducing aerosol removal through wet deposition. The convolution of the wind vertical structure with aerosol transport can then also help explain the abrupt reduction in the presence of boundary layer smoke in September, when more of the aerosol is aloft within stronger winds (Adebiyi and Zuidema, 2016; Shinozuka et al., 2019).

The question arises as to whether the net radiative impact is dominated by the aerosol, or by the accompanying reduction in daytime cloud fraction. Overall the top-of-atmosphere all-sky albedos decrease (Fig. S4, the difference is significant at the 90% level) as the smoke loading in the boundary layer increases, with the exception of 31 August, 2016. On this day, both the large-scale low-cloud fraction ($\sim$ 0.9) and albedo (near 0.4) are high. The high all-sky albedo may reflect an aerosol indirect effect (e.g., Lu et al., 2018), as ORACLES aircraft measurements to the southeast indicated little smoke in the free troposphere. This analysis primarily serves to indicate the possibility that a boundary layer semi-direct effect can be the dominant aerosol-cloud interactions at times, and to stimulate further research on this. A caveat is that this study is not able to say much about the presence of smoke within the free troposphere above the low-cloud deck accompanying either composite.

Adebiyi and Zuidema (2018) found that a decrease in low-cloud cover is associated with an increase in 800 hPa subsidence, a decrease in total column aerosol optical depth, and an increase in 600 hPa moisture, all else equal, for the July-October time span at this location. This analysis finds a stronger 800 hPa subsidence (not shown) and a possible increase in 600 hPa moisture (based on the vertical distributions of lidar extinction profiles and radiosonde q_v profiles, not shown) under less

5 cloudy conditions, and that smaller cloud fractions are likely associated with an increase in aerosol optical depth (not shown, but consistent with more smoke in the boundary layer). The Adebiyi and Zuidema (2018) analysis was not broken down by month at the Ascension Island location, and the small sample size of this study does not support a similar separation of variables. Further work will be needed to reconcile the apparent contrast between the two studies.

Why is understanding the diurnal cycle of this regime important? The altered phasing of the diurnal cycle with more smoke

10 present in the boundary layer impacts the daytime-mean cloud fraction, and thereby the net radiative impact. We hypothesize processes associated with the mid-morning boundary layer deepening that can only be fully teased out with modeling studies, ones which are also important for the stratocumulus-to-cumulus transition. The diurnal cycle is well-observed and its simulation can serve to develop confidence in a model's skill before modeling more challenging scenarios for which observations may not exist. The data analyzed here suggest a different mechanism by which the prevailing low-cloud types interact with the presence

15 of boundary layer smoke aerosol, presenting a new challenge for models with confidence in their representations of clouds and cloud-aerosol interactions. Salient aspects of the diurnal cycle are summarized in the schematic of Fig. 18.

Data availability. All the data are publicly-available through the Atmospheric Radiation Measurement Data Archive. The MPL extinction profiles are available upon request.

Appendix A

20 Among the 357 successfully launched radiosonde profiles during August 2016 and August 2017, two were aborted below 3000 meters, and thus, they were excluded from the subsequent analyses. Further quality controls revealed 2 bad wind profiles and 30 profiles that had an issue in relative humidity measurement (anomalously low RH, less than 10 %) in the first 500 m of the boundary layer, however, other variables associated with those profiles turned out to be valid, which were kept in the analyses. Out of those 355 profiles included in the analyses, 114 profiles were identified as daytime soundings and 126 were identified as

25 nighttime soundings. 0530 UTC (0430 LST) and 1730 UTC (1630 LST) launches were treated neither daytime nor nighttime to avoid potential confusion on whether the boundary layer was sunlit or not. The conditional composite method discussed above yields a total of 92 smoky radiosonde profiles (33 daytime and 38 nighttime) and 63 less smoky profiles (24 daytime and 23 nighttime) in 2016, and 29 smoky radiosonde profiles (7 daytime and 8 nighttime) and 27 less smoky profiles (7 daytime and 9 nighttime) in 2017, out of the 355 profiles. The radiosonde launching time was recorded in UTC, but shown here in LST,

30 which is approximately one hour earlier, to be consistent with the time stamps of the other measurements. The calculation of

the lifting condensation levels follows equations (4.6.23) to (4.6.25) in Emanuel (1994) using an air parcel originating from 1000 hPa.

Author contributions. JZ and PZ conceived the study. JZ performed the data analysis with help from PZ. JZ wrote the paper with reviews and edits from PZ.

Acknowledgements. The LASIC deployment of the ARM Mobile Facility was supported by the U.S. Department of Energy (DOE) Atmospheric Radiation Measurement Program (ARM) Climate Research Facility, funded by the U.S. Department of Energy's Office of Science, Office of Biological and Environmental Research as part of the Atmospheric Science Research Program. We are indebted to the scientists, instrument mentors, and logistics staff who made this analysis possible through their efforts in deploying and maintaining the instruments, and processing and calibrating the campaign datasets. This work was primarily supported by DOE ASR grant DE–SC0018272, with PZ acknowledging further support from NASA EVS-2 ORACLES grant NNX15AF98G. We thank Paul Barrett and Steve Abel for sharing the aircraft data from CLARIFY flight C030 and constructive discussions. The MODIS datasets are available through the NASA Level-3 Atmosphere Archive & Distribution System (LAADS) Distributed Active Archive Center (DAAC). The CERES and SEVIRI retrievals are available from NASA Langley Research Center, with Douglas Spangenberg serving as contact for developing the SEVIRI retrievals.The 5th generation ECMWF atmospheric reanalyses of the global climate data are available on Copernicus Climate Change Service (C3S). The UK Met Office SYNOP hourly weather reports are available on the CEDA archive through the Met Office Integrated Data Archive System (MIDAS). We thank three anonymous reviewers for constructive criticism that encouraged us to think more deeply about our analysis.

References

Ackerman, A. S., Toon, O. B., Stevens, D. E., Heymsfield, A. J., Ramanathan, V., and Welton, E. J.: Reduction of tropical cloudiness by soot, Science, 288, 1042–1047, https://doi.org/doi: 10.1126/science.288.5468.1042, 2000.

Adebiyi, A. A. and Zuidema, P.: The role of the southern African easterly jet in modifying the southeast Atlantic aerosol and cloud environments, Q. J. Roy. Meteor.Soc., 142, 1574–1589, https://doi.org/10.1002/qj.2765, 2016.

Adebiyi, A. A. and Zuidema, P.: Low Cloud Cover Sensitivity to Biomass-Burning Aerosols and Meteorology over the Southeast Atlantic, J. Climate, 31, 4329–4346, https://doi.org/10.1175/JCLI-D-17-0406.1, 2018.

Adebiyi, A. A., Zuidema, P., and Abel, S. J.: The Convolution of Dynamics and Moisture with the Presence of Shortwave Absorbing Aerosols over the Southeast Atlantic, J. Climate, 28, 1997–2024, https://doi.org/10.1175/JCLI-D-14-00352.1, 2015.

Allen, G., Coe, H., Clarke, A., Bretherton, C., Wood, R., Abel, S. J., Barrett, P., Brown, P., George, R., Freitag, S., McNaughton, C., Howell, S., Shank, L., Kapustin, V., Brekhovskikh, V., Kleinman, L., Lee, Y.-N., Springston, S., Toniazzo, T., Krejci, R., Fochesatto, J., Shaw, G., Krecl, P., Brooks, B., McMeeking, G., Bower, K. N., Williams, P. I., Crosier, J., Crawford, I., Connolly, P., Allan, J. D., Covert, D., Bandy, A. R., Russell, L. M., Trembath, J., Bart, M., McQuaid, J. B., Wang, J., and Chand, D.: South East Pacific atmospheric composition and variability sampled along 20° S during VOCALS-REx, Atmos. Chem. Phys., 11, 5237–5262, https://doi.org/10.5194/acp-11-5237-2011, 2011.

Burleyson, C. D. and Yuter, S. E.: Subdiurnal Stratocumulus Cloud Fraction Variability and Sensitivity to Precipitation, J. Climate, 28, 2968–2985, https://doi.org/10.1175/JCLI-D-14-00648.1, 2015.

Chellappan, S., Meirink, J. F., Horváth, Á., Bennartz, R., and Roebeling, R.: Evaluating the diurnal cycle of South Atlantic stratocumulus clouds as observed by MSG SEVIRI, Atmos. Chem. Phys., 18, 13 283–13 304, https://doi.org/10.5194/acp-18-13283-2018, 2018.

Ciesielski, P. E., Schubert, W. H., and Johnson, R. H.: Diurnal Variability of the Marine Boundary Layer during ASTEX, J. Atmos. Sci., 58, 2355–2376, https://doi.org/10.1175/1520-0469(2001)058<2355:DVOTMB>2.0.CO;2, 2001.

Cochrane, S. P., Schmidt, K. S., Chen, H., Pilewskie, P., Kittelman, S., Redemann, J., LeBlanc, S., Pistone, K., Kacenelenbogen, M., Segal Rozenhaimer, M., Shinozuka, Y., Flynn, C., Platnick, S., Meyer, K., Ferrare, R., Burton, S., Hostetler, C., Howell, S., Dobracki, A., and Doherty, S.: Above-Cloud Aerosol Radiative Effects based on ORACLES 2016 and ORACLES 2017 Aircraft Experiments, Atmos. Meas. Tech. Discuss., in review, https://doi.org/10.5194/amt-2019-125, 2019.

Costantino, L. and Bréon, F.-M.: Aerosol indirect effect on warm clouds over South-East Atlantic, from co-located MODIS and CALIPSO observations, Atmos. Chem. Phys., 13, 69 – 88, https://doi.org/10.5194/acp-13-69-2013, 2013.

Das, S., Harshvardhan, H., Bian, H., Chin, M., Curci, G., Protonotariou, A. P., Mielonen, T., Zhang, K., Wang, H., and Liu, X.: Biomass burning aerosol transport and vertical distribution over the South African-Atlantic region, J. Geophys. Res. Atmos., 122, 6391–6415, https://doi.org/10.1002/2016JD026421, 2017.

Deaconu, L. T., Ferlay, N., Waquet, F., Peers, F., Thieuleux, F., and Goloub, P.: Satellite inference of water vapor and aerosol-above-cloud combined effect on radiative budget and cloud top processes in the Southeast Atlantic Ocean, Atmos. Chem. Phys. Discuss., in review, https://doi.org/10.5194/acp-2019-189, 2019.

Delgadillo, R., Voss, K. J., and Zuidema, P.: Characteristics of Optically Thin Coastal Florida Cumuli Derived From Surface-Based Lidar Measurements, J. Geophys. Res. Atmos., 123, 10,591–10,605, https://doi.org/10.1029/2018JD028867, 2018.

Diamond, M. S., Dobracki, A., Freitag, S., Small Griswold, J. D., Heikkila, A., Howell, S. G., Kacarab, M. E., Podolske, J. R., Saide, P. E., and Wood, R.: Time-dependent entrainment of smoke presents an observational challenge for assessing aerosol–cloud interactions over the southeast Atlantic Ocean, Atmos. Chem. Phys., 18, 14 623–14 636, https://doi.org/10.5194/acp-18-14623-2018, 2018.

Eastman, R. and Warren, S. G.: Diurnal Cycles of Cumulus, Cumulonimbus, Stratus, Stratocumulus, and Fog from Surface Observations over Land and Ocean, J. Climate, 27, 2386–2404, https://doi.org/10.1175/JCLI-D-13-00352.1, 2014.

Emanuel, K. A.: Atmospheric Convection, 13, Oxford University Press, 1 edn., 1994.

Fuchs, J., Cermak, J., and Andersen, H.: Building a cloud in the southeast Atlantic: understanding low-cloud controls based on satellite observations with machine learning, Atmos. Chem. Phys., 18, 16 537–16 552, https://doi.org/10.5194/acp-18-16537-2018, 2018.

Garstang, M., Tyson, P. D., Swap, R., Edwards, M., Kållberg, P., and Lindesay, J. A.: Horizontal and vertical transport of air over southern Africa, J. Geophys. Res. Atmos., 101, 23 721–23 736, https://doi.org/10.1029/95JD00844, 1996.

Gordon, H., Field, P. R., Abel, S. J., Dalvi, M., Grosvenor, D. P., Hill, A. A., Johnson, B. T., Miltenberger, A. K., Yoshioka, M., and Carslaw, K. S.: Large simulated radiative effects of smoke in the south-east Atlantic, Atmos. Chem. Phys., 18, 15 261–15 289, https://doi.org/10.5194/acp-18-15261-2018, 2018.

Grosvenor, D. P., Sourdeval, O., Zuidema, P., Ackerman, A., Alexandrov, M. D., Bennartz, R., Boers, R., Cairns, B., Chiu, J. C., Christensen, M., Deneke, H., Diamond, M., Feingold, G., Fridlind, A., Hünerbein, A., Knist, C., Kollias, P., Marshak, A., McCoy, D., Merk, D., Painemal, D., Rausch, J., Rosenfeld, D., Russchenberg, H., Seifert, P., Sinclair, K., Stier, P., van Diedenhoven, B., Wendisch, M., Werner, F., Wood, R., Zhang, Z., and Quaas, J.: Remote Sensing of Droplet Number Concentration in Warm Clouds: A Review of the Current State of Knowledge and Perspectives, Rev. Geophys., 56, 409–453, https://doi.org/10.1029/2017RG000593, 2018.

Hansen, J., Sato, M., Lacis, A., and Ruedy, R.: The missing climate forcing, Phil. Trans. Roy. Soc. B, 352, 231– 240, https://doi.org/10.1098/rstb.1997.0018, 1997.

Haywood, J. M., Osborne, S. R., Francis, P. N., Keil, A., Formenti, P., Andreae, M. O., and Kaye, P. H.: The mean physical and optical properties of regional haze dominated by biomass burning aerosol measured from the C-130 aircraft during SAFARI 2000, J. Geophys. Res. Atmos., 108, https://doi.org/10.1029/2002JD002226, 2003.

Herbert, R. J., Bellouin, N., Highwood, E. J., and Hill, A. A.: Diurnal cycle of the semi–direct effect over marine stratocumulus in large–eddy simulations, Atmos. Chem. Phys. Discuss., in review, https://doi.org/10.5194/acp-2019-387, 2019.

Hignett, P.: Observations of Diurnal Variation in a Cloud-capped Marine Boundary Layer, J. Atmos. Sci., 48, 1474–1482, https://doi.org/10.1175/1520-0469(1991)048<1474:OODVIA>2.0.CO;2, 1991.

Johnson, B. T., Shine, K. P., and Forster, P. M.: The semi-direct aerosol effect: Impact of absorbing aerosols on marine stratocumulus, Q. J. R. Meteorol. Soc., 130, 1407–1422, https://doi.org/10.1256/qj.03.61, 2004.

Klein, S. A., Hartmann, D. L., and Norris, J. R.: On the Relationships among Low-Cloud Structure, Sea Surface Temperature, and Atmospheric Circulation in the Summertime Northeast Pacific, J. Climate, 8, 1140–1155, https://doi.org/10.1175/1520-0442(1995)008<1140:OTRALC>2.0.CO;2, 1995.

Koch, D. and Del Genio, A. D.: Black carbon semi-direct effects on cloud cover: review and synthesis, Atmos. Chem. Phys., 10, 7685–7696, https://doi.org/10.5194/acp-10-7685-2010, 2010.

LeBlanc, S. E., Redemann, J., Flynn, C., Pistone, K., Kacenelenbogen, M., Segal-Rosenheimer, M., Shinozuka, Y., Dunagan, S., Dahlgren, R. P., Meyer, K., Podolske, J., Howell, S. G., Freitag, S., Small-Griswold, J., Holben, B., Diamond, M., Formenti, P., Piketh, S., Maggs-Kölling, G., Gerber, M., and Namwoonde, A.: Above Cloud Aerosol Optical Depth from airborne observations in the South-East Atlantic, Atmos. Chem. Phys. Discuss., in review, https://doi.org/10.5194/acp-2019-43, 2019.

Lu, Z., Liu, X., Zhang, Z., Zhao, C., Meyer, K., Rajapakshe, C., Wu, C., Yang, Z., and Penner, J. E.: Biomass smoke from southern Africa can significantly enhance the brightness of stratocumulus over the southeastern Atlantic Ocean, Proc. Natl. Acad. Sci., 115, 2924–2929, https://doi.org/10.1073/pnas.1713703115, 2018.

Miller, M. A. and Albrecht, B. A.: Surface Based Observations of Mesoscale Cumulus Stratocumulus Interaction during ASTEX, J. Atmos. Sci., 52, 2809–2826, https://doi.org/10.1175/1520-0469(1995)052<2809:SBOOMC>2.0.CO;2, 1995.

Miller, M. A., Jensen, M. P., and Clothiaux, E. E.: Diurnal Cloud and Thermodynamic Variations in the Stratocumulus Transition Regime: A Case Study Using In Situ and Remote Sensors, J. Atmos. Sci., 55, 2294–2310, https://doi.org/10.1175/1520-0469(1998)055<2294:DCATVI>2.0.CO;2, 1998.

Miller, M. A., Nitschke, K., Ackerman, T. P., Ferrell, W. R., Hickmon, N., and Ivey, M.: The ARM Mobile Facilities, Meteorological Monographs, 57, 9.1–9.15, https://doi.org/10.1175/AMSMONOGRAPHS-D-15-0051.1, 2016.

Minnis, P., Nguyen, L., Palikonda, R., Heck, P. W., Spangenberg, D. A., Doelling, D. R., Kirk Ayers, J., Smith, W. L., Khaiyer, M. M., Trepte, Q. Z., Avey, L. A., Chang, F.-L., Yost, C. R., Chee, T. L., and Szedung, T. L.: Near-real time cloud retrievals from operational and research meteorological satellites, Proc. Vol. Remote Sensing of Clouds and the Atmosphere XIII, 7107, 710703, https://doi.org/10.1117/12.800344, 2008.

Minnis, P., Sun-Mack, S., Young, D. F., Heck, P. W., Garber, D. P., Chen, Y., Spangenberg, D. A., Arduini, R. F., Trepte, Q. Z., Smith, W. L., Ayers, J. K., Gibson, S. C., Miller, W. F., Hong, G., Chakrapani, V., Takano, Y., Liou, K., Xie, Y., and Yang, P.: CERES Edition-2 Cloud Property Retrievals Using TRMM VIRS and Terra and Aqua MODIS Data–Part I: Algorithms, IEEE Trans. Geosci. Remote Sens., 49, 4374–4400, https://doi.org/10.1109/TGRS.2011.2144601, 2011.

Painemal, D., Garreaud, R., Rutllant, J., and Zuidema, P.: Southeast Pacific Stratocumulus: High-Frequency Variability and Mesoscale Structures over San Félix Island, J. Appl. Meteor. Climatol., 49, 463–477, https://doi.org/10.1175/2009JAMC2230.1, 2010.

Painemal, D., Kato, S., and Minnis, P.: Boundary layer regulation in the southeast Atlantic cloud microphysics during the biomass burning season as seen by the A-train satellite constellation, J. Geophys. Res. Atmos., 119, 11 288–11 302, https://doi.org/10.1002/2014JD022182, 2014.

Painemal, D., Xu, K.-M., Cheng, A., Minnis, P., and Palikonda, R.: Mean Structure and Diurnal Cycle of Southeast Atlantic Boundary Layer Clouds: Insights from Satellite Observations and Multiscale Modeling Framework Simulations, J. Climate, 28, 324–341, https://doi.org/10.1175/JCLI-D-14-00368.1, 2015.

Peers, F., Waquet, F., Cornet, C., Dubuisson, P., Ducos, F., Goloub, P., Szczap, F., Tanré, D., and Thieuleux, F.: Absorption of aerosols above clouds from POLDER/PARASOL measurements and estimation of their direct radiative effect, Atmos. Chem. Phys., 15, 4179–4196, https://doi.org/10.5194/acp-15-4179-2015, 2015.

Peers, F., Francis, P., Fox, C., Abel, S. J., Szpek, K., Cotterell, M. I., Davies, N. W., Langridge, J. M., Meyer, K. G., Platnick, S. E., and Haywood, J. M.: Observation of absorbing aerosols above clouds over the South- East Atlantic Ocean from the geostationary satellite SEVIRI – Part 1: Method description and sensitivity, Atmos. Chem. Phys., 19, 9595–9611, https://doi.org/10.5194/acp-19-9595-2019, 2019.

Pennypacker, S., Diamond, M., and Wood, R.: Ultra-clean and smoky marine boundary layers frequently occur in the same season over the southeast Atlantic, Atmos. Chem. Phys. Discuss., in review, https://doi.org/10.5194/acp-2019-628, 2019.

Pistone, K., Praveen, P. S., Thomas, R. M., Ramanathan, V., Wilcox, E. M., and Bender, F. A.-M.: Observed correlations between aerosol and cloud properties in an Indian Ocean trade cumulus regime, Atmos. Chem. Phys., 16, 5203–5227, https://doi.org/10.5194/acp-16-5203-2016, 2016.

Pistone, K., Redemann, J., Doherty, S., Zuidema, P., Burton, S., Cairns, B., Cochrane, S., Ferrare, R., Flynn, C., Freitag, S., Howell, S., Kacenelenbogen, M., LeBlanc, S., Liu, X., Schmidt, K. S., Sedlacek III, A. J., Segal-Rosenhaimer, M., Shinozuka, Y., Stamnes, S., van Diedenhoven, B., Van Harten, G., and Xu, F.: Intercomparison of biomass burning aerosol optical properties from in-situ and remote-sensing instruments in ORACLES-2016, Atmos. Chem. Phys., 19, 9181–9208, https://doi.org/10.5194/acp-19-9181-2019, 2019.

5 Platnick, S. and coauthors: MODIS Atmosphere L3 Monthly Product, NASA MODIS Adaptive Processing System, Goddard Space Flight Center, https://doi.org/10.5067/MODIS/MOD08_M3.061, 2017.

Rémillard, J., Kollias, P., Luke, E., and Wood, R.: Marine Boundary Layer Cloud Observations in the Azores, J. Climate, 25, 7381–7398, https://doi.org/10.1175/JCLI-D-11-00610.1, 2012.

Rozendaal, M. A., Leovy, C. B., and Klein, S. A.: An Observational Study of Diurnal Variations of Marine Stratiform Cloud, J. Climate, 8,
10 1795–1809, https://doi.org/10.1175/1520-0442(1995)008<1795:AOSODV>2.0.CO;2, 1995.

Sayer, A. M., Hsu, N. C., Lee, J., Kim, W. V., Burton, S., Fenn, M. A., Ferrare, R. A., Kacenelenbogen, M., LeBlanc, S., Pistone, K., Redemann, J., Segal-Rozenhaimer, M., Shinozuka, Y., and Tsay, S.-C.: Two decades observing smoke above clouds in the south-eastern Atlantic Ocean: Deep Blue algorithm updates and validation with ORACLES field campaign data, Atmos. Meas. Tech., 12, 3595–3627, https://doi.org/10.5194/amt-12-3595-2019, 2019.

15 Shank, L. M., Howell, S., Clarke, A. D., Freitag, S., Brekhovskikh, V., Kapustin, V., McNaughton, C., Campos, T., and Wood, R.: Organic matter and non-refractory aerosol over the remote Southeast Pacific: oceanic and combustion sources, Atmos. Chem. Phys., 12, 557–576, https://doi.org/10.5194/acp-12-557-2012, 2012.

Shinozuka, Y., Saide, P. E., Ferrada, G. A., Burton, S. P., Ferrare, R., Doherty, S. J., Gordon, H., Longo, K., Mallet, M., Feng, Y., Wang, Q., Cheng, Y., Dobracki, A., Freitag, S., Howell, S. G., LeBlanc, S., Flynn, C., Segal-Rosenhaimer, M., Pistone, K., Podolske, J. R., Stith,
20 E. J., Bennett, J. R., Carmichael, G. R., da Silva, A., Govindaraju, R., Leung, R., Zhang, Y., Pfister, L., Ryoo, J.-M., Redemann, J., Wood, R., and Zuidema, P.: Modeling the smoky troposphere of the southeast Atlantic: a comparison to ORACLES airborne observations from September of 2016, Atmos. Chem. Phys. Discuss., in review, https://doi.org/10.5194/acp-2019-678, 2019.

Stevens, B.: On the Growth of Layers of Nonprecipitating Cumulus Convection, J. Atmos. Sci., 64, 2916–2931, https://doi.org/10.1175/JAS3983.1, 2007.

25 Stevens, B. and Seifert, A.: Understanding macrophysical outcomes of microphysical choices in simulations of shallow cumulus convection, J. Meteor. Soc. Japan, 86A, 143–162, 2008.

Turner, D. D., Clough, S. A., Liljegren, J. C., Clothiaux, E. E., Cady-Pereira, K. E., and Gaustad, K. L.: Retrieving liquid water path and precipitable water vapor from the atmospheric radiation measurement (ARM) microwave radiometers, IEEE Trans. Geos. Remote Sens., 45, 3680–3689, https://doi.org/10.1109/TGRS.2007.903703, 2007.

30 Waquet, F., Peers, F., Ducos, F., Goloub, P., Platnick, S., Riedi, J., Tanré, D., and Thieuleux, F.: Global analysis of aerosol properties above clouds, Geophys. Res. Lett., 40, 5809–5814, https://doi.org/10.1002/2013GL057482, 2013.

Wilcox, E. M.: Stratocumulus cloud thickening beneath layers of absorbing smoke aerosol, Atmos. Chem. Phys., 10, 11 769 – 11 777, 2010.

Wilcox, E. M.: Direct and semi-direct radiative forcing of smoke aerosols over clouds, Atmos. Chem. Phys., 12, 139–149, https://doi.org/10.5194/acp-12-139-2012, 2012.

35 Wilcox, E. M., Thomas, R. M., Praveen, P. S., Pistone, K., Bender, F. A.-M., and Ramanathan, V.: Black carbon solar absorption suppresses turbulence in the atmospheric boundary layer, Proc. Natl. Acad. Sci., 113, 11 794–11 799, https://doi.org/10.1073/pnas.1525746113, 2016.

WMO: Manual on Codes, 306, World Meteorological Organization Publ., 1 edn., 1974.

Wood, R., Stemmler, J. D., Rémillard, J., and Jefferson, A.: Low-CCN concentration air masses over the eastern North Atlantic: Seasonality, meteorology, and drivers, J. Geophys. Res. Atmos., 122, 1203–1223, https://doi.org/10.1002/2016JD025557, 2017.

Yamaguchi, T., Feingold, G., Kazil, J., and McComiskey, A.: Stratocumulus to cumulus transition in the presence of elevated smoke layers, Geophys. Res. Lett., 42, 10 478–10 485, https://doi.org/10.1002/2015GL066544, 2015.

5 Yin, B. and Albrecht, B. A.: Spatial Variability of Atmospheric Boundary Layer Structure over the Eastern Equatorial Pacific, J. Climate, 13, 1574–1592, https://doi.org/10.1175/1520-0442(2000)013<1574:SVOABL>2.0.CO;2, 2000.

Zhou, X., Ackerman, A. S., Fridlind, A. M., Wood, R., and Kollias, P.: Impacts of solar-absorbing aerosol layers on the transition of stratocumulus to trade cumulus clouds, Atmos. Chem. Phys., 17, 12 725–12 742, https://doi.org/10.5194/acp-17-12725-2017, 2017.

Zuidema, P., Chiu, C., Fairall, C., Ghan, S., Kollias, P., McFarguhar, G., Mechem, D., Romps, D., Wong, H., Yuter, S., Alvarado, M.,
10 DeSzoeke, S., Feingold, G., Haywood, J., Lewis, E., McComiskey, A., Redemann, J., Turner, D., Wood, R., and Zhu, P.: Layered Atlantic Smoke Interactions with Clouds (LASIC) Science Plan: DOE Office of Science Atmospheric Radiation Measurement (ARM) Program, http://www.osti.gov/scitech/servlets/purl/1232658, 2015.

Zuidema, P., Chang, P., Medeiros, B., Kirtman, B. P., Mechoso, R., Schneider, E. K., Toniazzo, T., Richter, I., Small, R. J., Bellomo, K., Brandt, P., de Szoeke, S., Farrar, J. T., Jung, E., Kato, S., Li, M., Patricola, C., Wang, Z., Wood, R., and Xu, Z.: Challenges and Prospects
15 for Reducing Coupled Climate Model SST Biases in the Eastern Tropical Atlantic and Pacific Oceans: The U.S. CLIVAR Eastern Tropical Oceans Synthesis Working Group, Bull. Amer. Meteor. Soc., 97, 2305–2328, https://doi.org/10.1175/BAMS-D-15-00274.1, 2016a.

Zuidema, P., Redemann, J., Haywood, J., Wood, R., Piketh, S., Hipondoka, M., and Formenti, P.: Smoke and Clouds above the Southeast Atlantic: Upcoming Field Campaigns Probe Absorbing Aerosol's Impact on Climate, Bull. Amer. Meteor. Soc., 97, 1131–1135, https://doi.org/10.1175/BAMS-D-15-00082.1, 2016b.

20 Zuidema, P., Sedlacek, A. J., Flynn, C., Springston, S., Delgadillo, R., Zhang, J., Aiken, A. C., Koontz, A., and Muradyan, P.: The Ascension Island Boundary Layer in the Remote Southeast Atlantic is Often Smoky, Geophys. Res. Lett., 45, 4456–4465, https://doi.org/10.1002/2017GL076926, 2018.
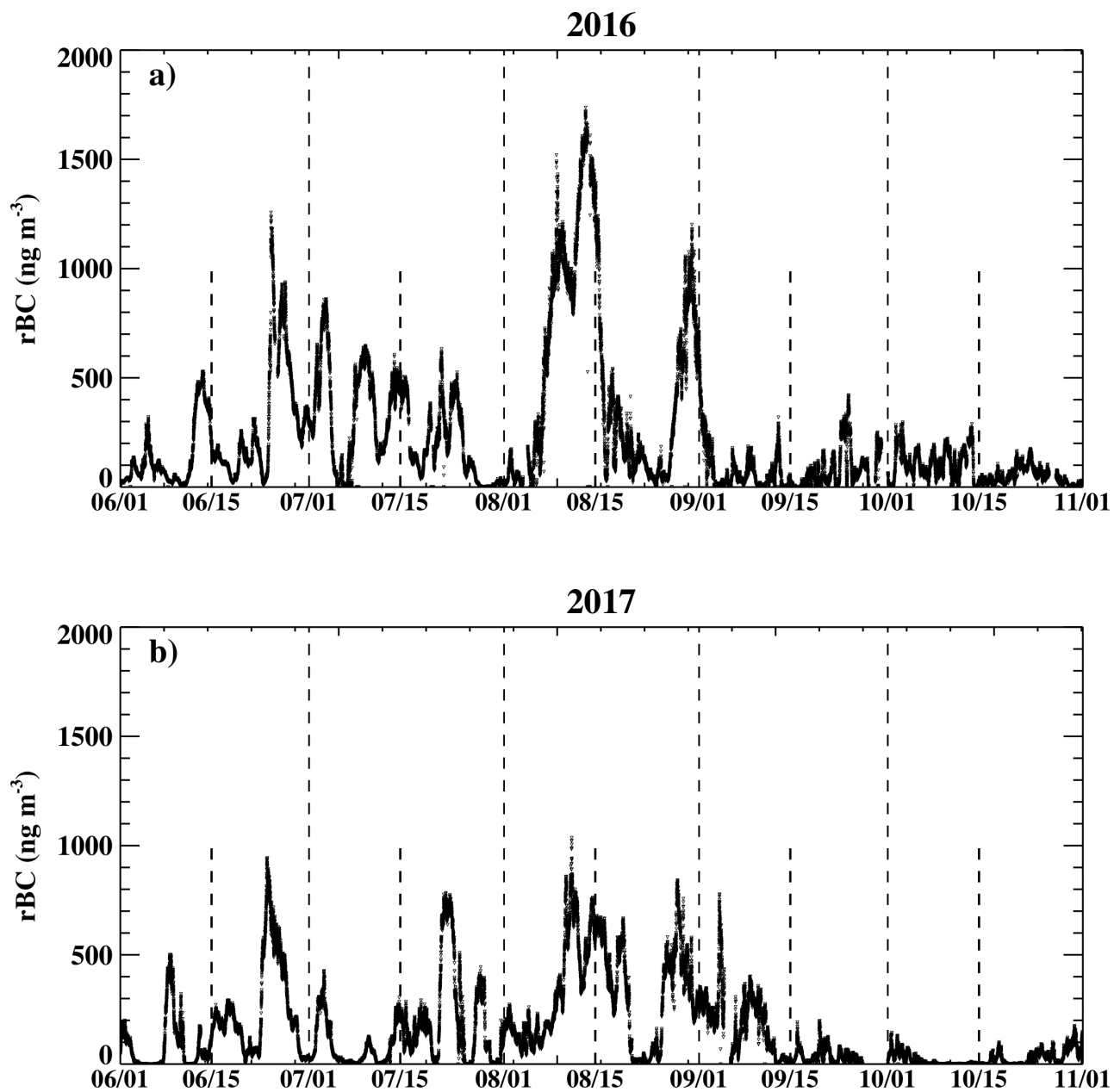
Figure 1. Time series of refractory black carbon (rBC) mass concentrations from 1 June to 31 October for a) 2016 and b) 2017.
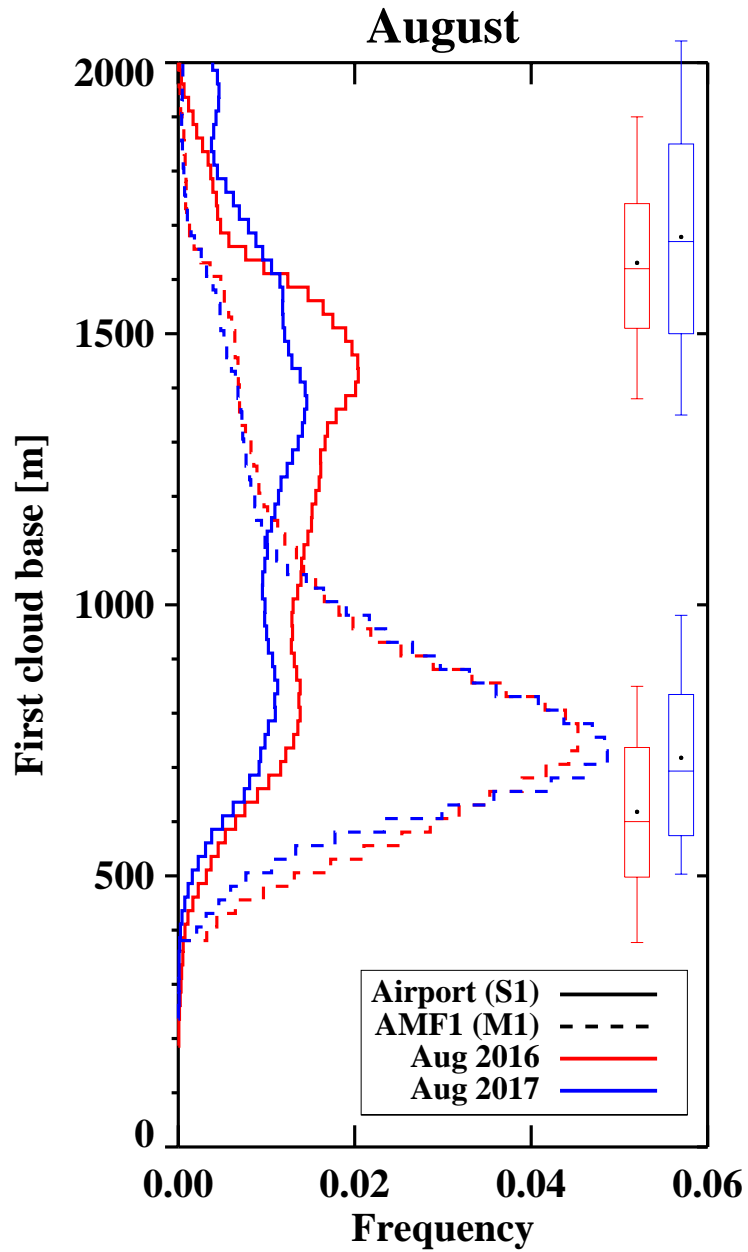
Figure 2. Normalized frequency distribution of the lowest ceilometer-derived cloud bases in August 2016 (red) and 2017 (blue) at the airport (solid) and AMF1 site (dashed). The median, 10th, 25th, 75th and 90th percentile values of the radiosonde-derived lifting condensation level and trade-wind inversion base are indicated for both years, with filled circles indicating the mean.
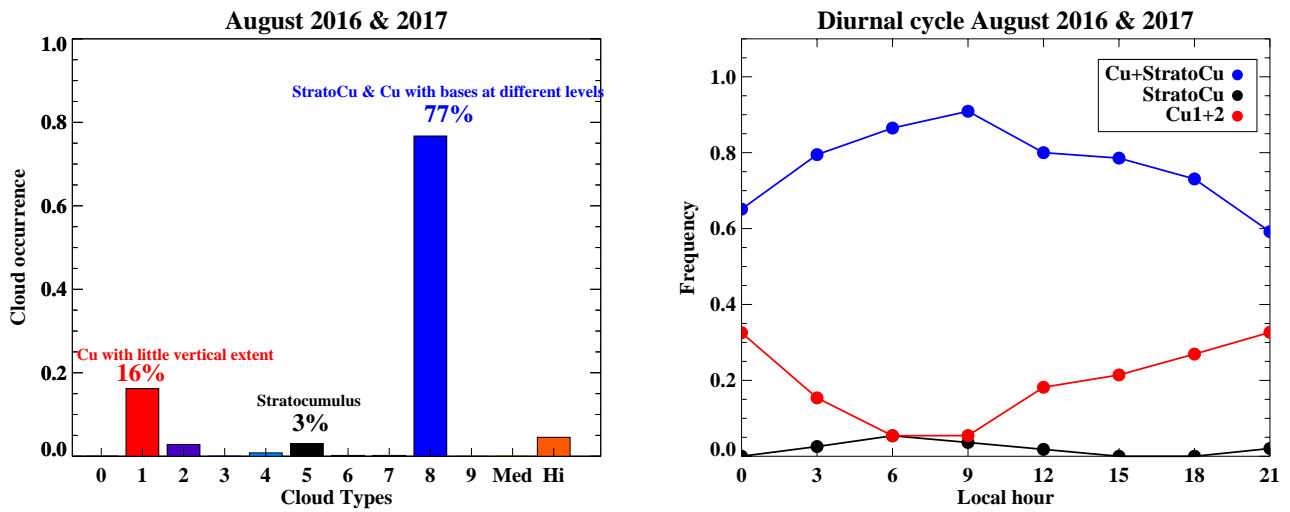
Figure 3. Left: Frequency of occurrence of the three-hourly cloud types reported by surface observers for both August months, and, right: the corresponding diurnal cycle of the dominant low cloud types. The cloud types are reported following World Meteorological Organization protocol: C_L=1,2 (red) represents "cumulus with little vertical extent" and "cumulus with moderate or strong vertical extent", C_L=5 (black), represents "stratocumulus", and C_L=8 (blue) represents "stratocumulus and cumulus with bases at different levels".
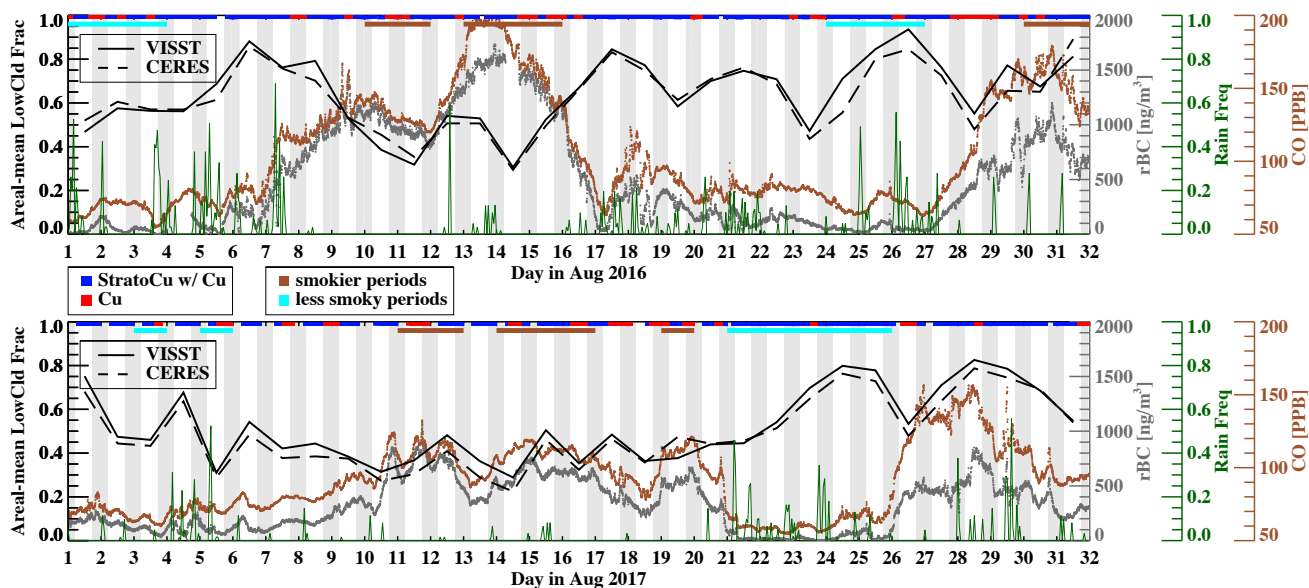
Figure 4. Upper panel: August 2016 time series of refractory black carbon mass and carbon monoxide concentrations (rBC and CO, grey and brown filled circles respectively) and disdrometer-derived hourly rain frequencies (dark green curves) at the AMF1 site, and daily low-cloud fractions averaged over 6°-10°S, 11°W-15°W. Bottom panel: Similar time series for August 2017. The daily-mean Meteosat10 VISST and CERES Terra and Aqua low-cloud fractions are indicated in solid and dashed black lines, respectively. The visual surface-based cloud classification is indicated above each panel, color-coded in red, for "cumulus of little vertical extent", and blue, for "stratocumulus and cumulus with bases at different levels". The "more" and "less" smoky days contributing to each group are also indicated above each panel, color-coded in brown and cyan, respectively.
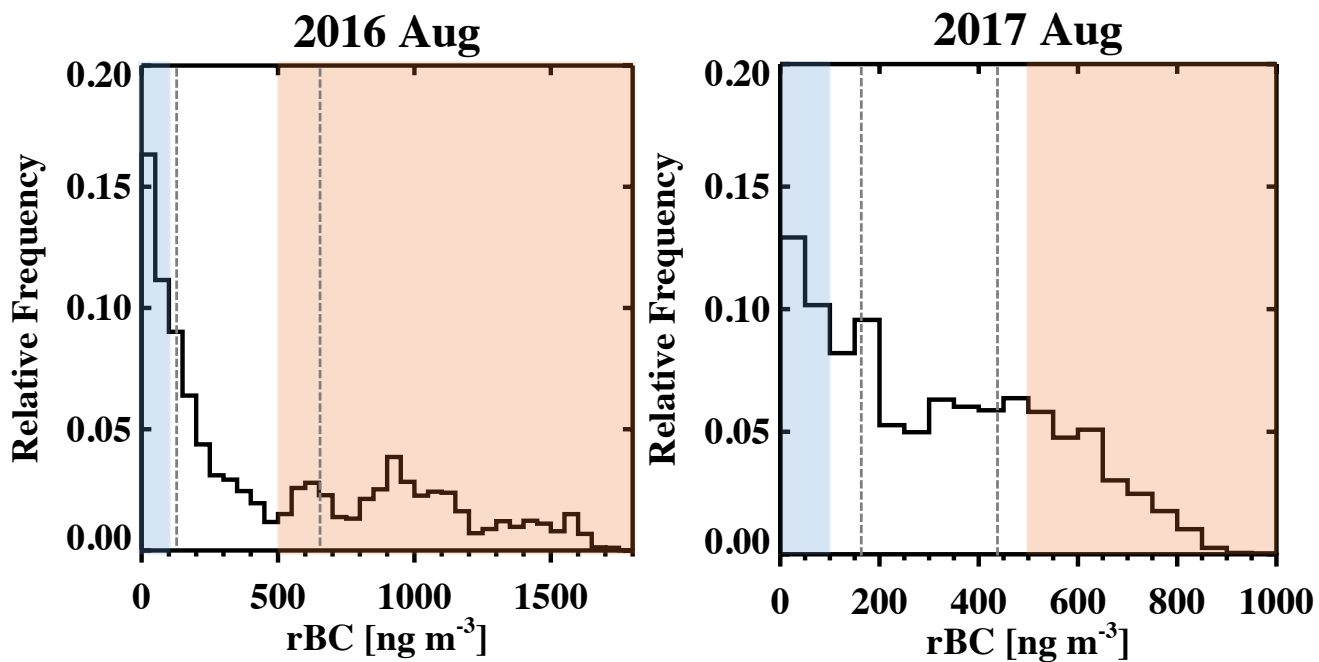
Figure 5. Histograms of one-minute refractory black carbon mass concentration at Ascension Island for August 2016 (left panel) and 2017 (right panel). Tercile values are indicated with gray dashed lines, and red and blue shadings indicate the daily thresholds selected for "more" and "less " smoky conditions.
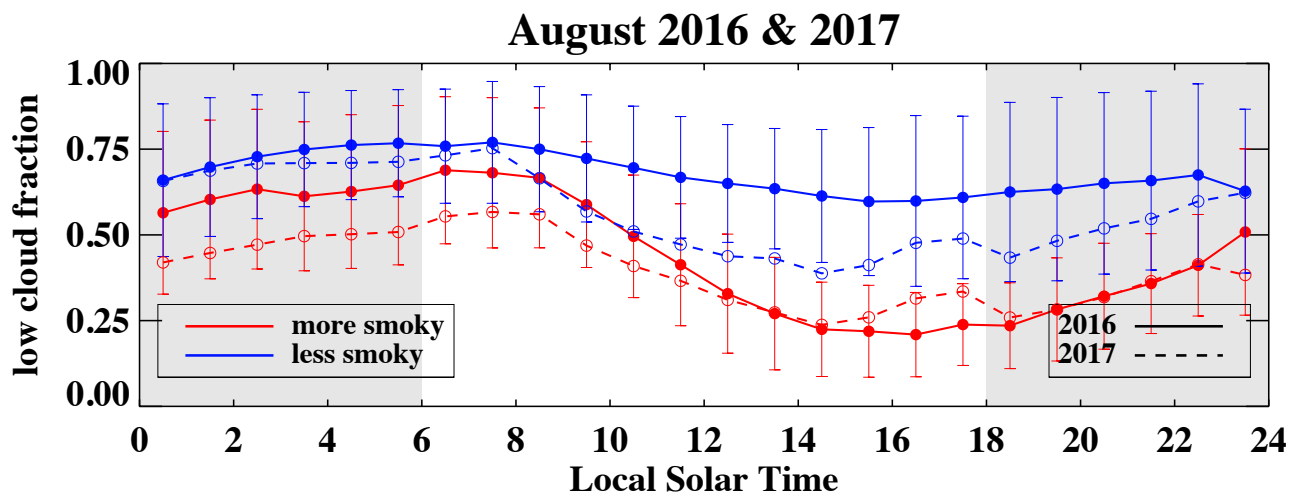
Figure 6. SEVIRI-derived hourly low-cloud fractions over 6°-10°S, 11°W-15°W, composited by "more" (red) and "less" (blue) smoky days, for August 2016 (solid line) and 2017 (dashed line). Shown are mean values and the standard deviation of each composite group for that hour. Gray shading indicates night time.
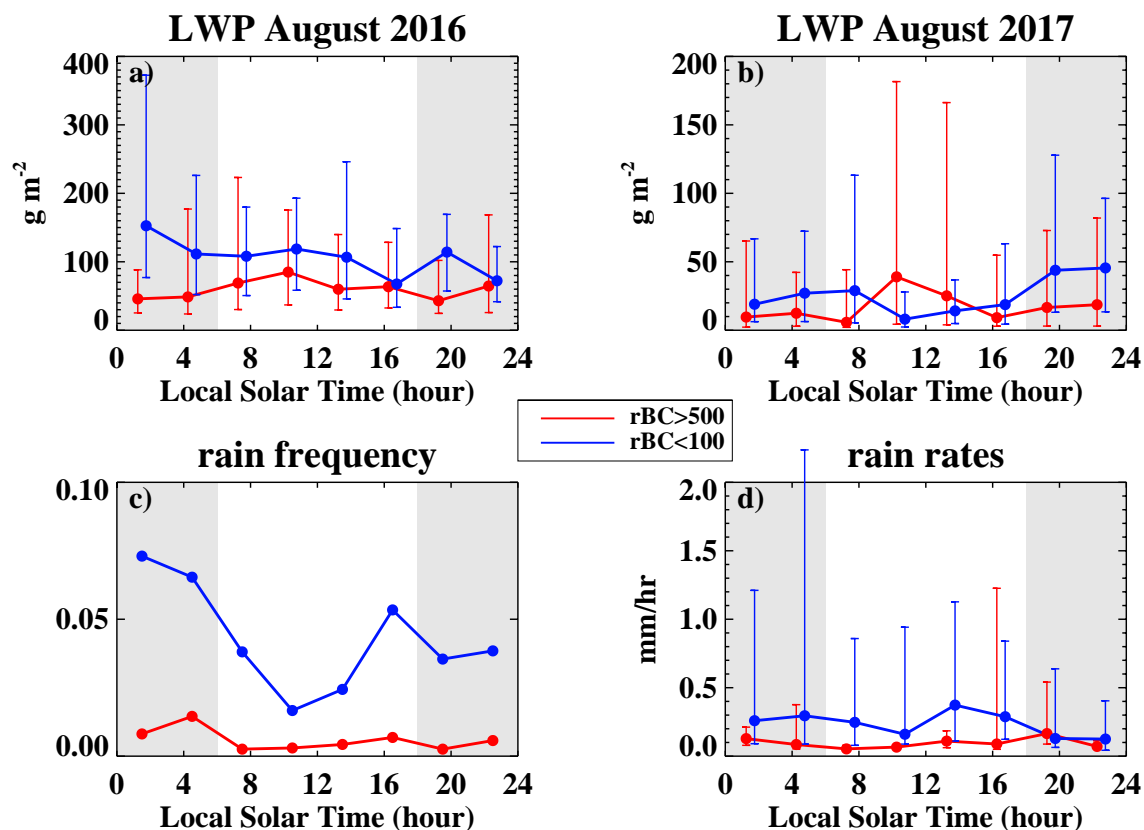
Figure 7. Diurnal cycle of liquid water paths at the airport for a) August 2016 and b) August 2017, composited by "more" (red) versus "less" (blue) smoky days, shown as the median values (filled circles) and interquartile range (vertical bars) of one-minute cloud LWP values > 0. Note the change in y-axis range between a) and b). c) Diurnal cycle of 3-hourly disdrometer-derived rain frequencies, 2016 and 2017 combined. d) Diurnal cycle in the median rain rates and their interquartile range at the AMF1 site, similarly composited for 2016 and 2017 combined. Only one-minute samples with rain rates exceeding 0 mm/hr are included. The data are aggregated every three hours (0-3, 3-6, 6-9, 9-12, 12-15, 15-18, 18-21, 21-24 LST) with values indicated approximately at their midpoint in time. Gray shadings indicate night time.
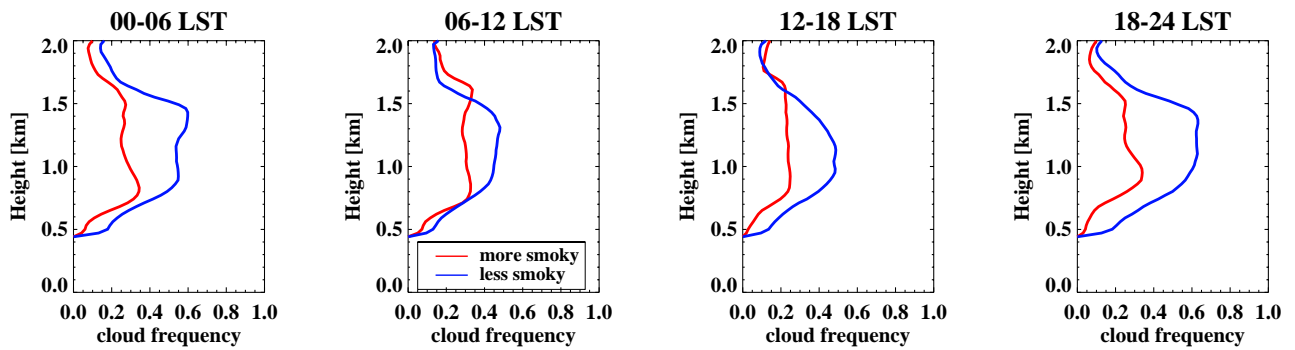
Figure 8. Diurnal cycle in the mean cloud frequencies derived using Ka-band zenith pointing cloud radar (KAZR) reflectivities > 35 dBZ at their vertical resolution of 30 m, composited by "more" (red) versus "less" (blue) smoky conditions from, left to right: 0-6 LST; 6-12 LST; 12-18 LST; and 18-24 LST.
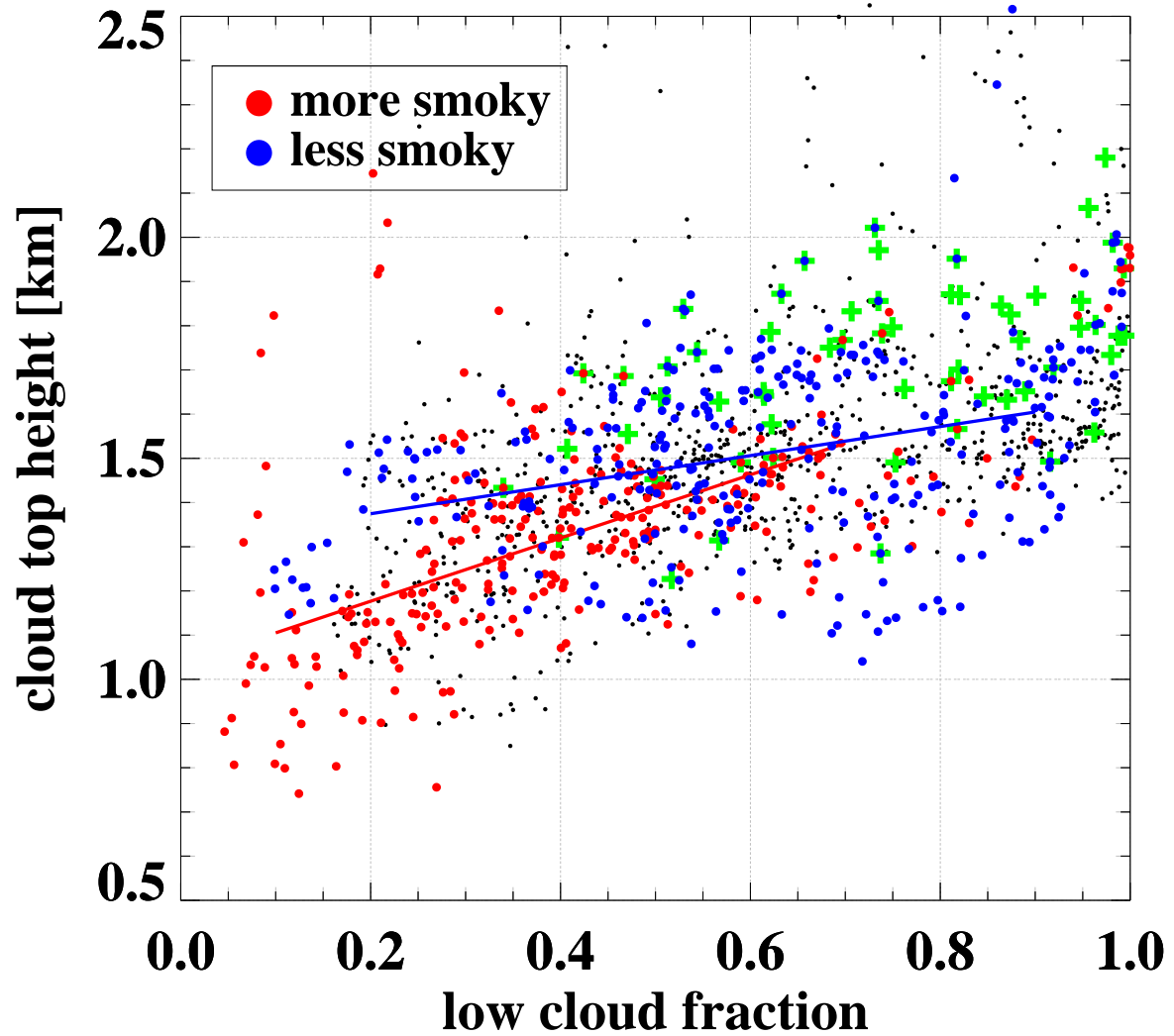
Figure 9. Hourly-mean SEVIRI-derived effective cloud top height as a function of low-cloud fractions over 6°-10°S, 11°W-15°W. Cloud top heights corresponding to "more" and "less" smoky conditions are indicated in red and blue, respectively, and include linear fits as a function of cloud fraction. 08 LST values are highlighted in green crosses regardless of smoke loading.
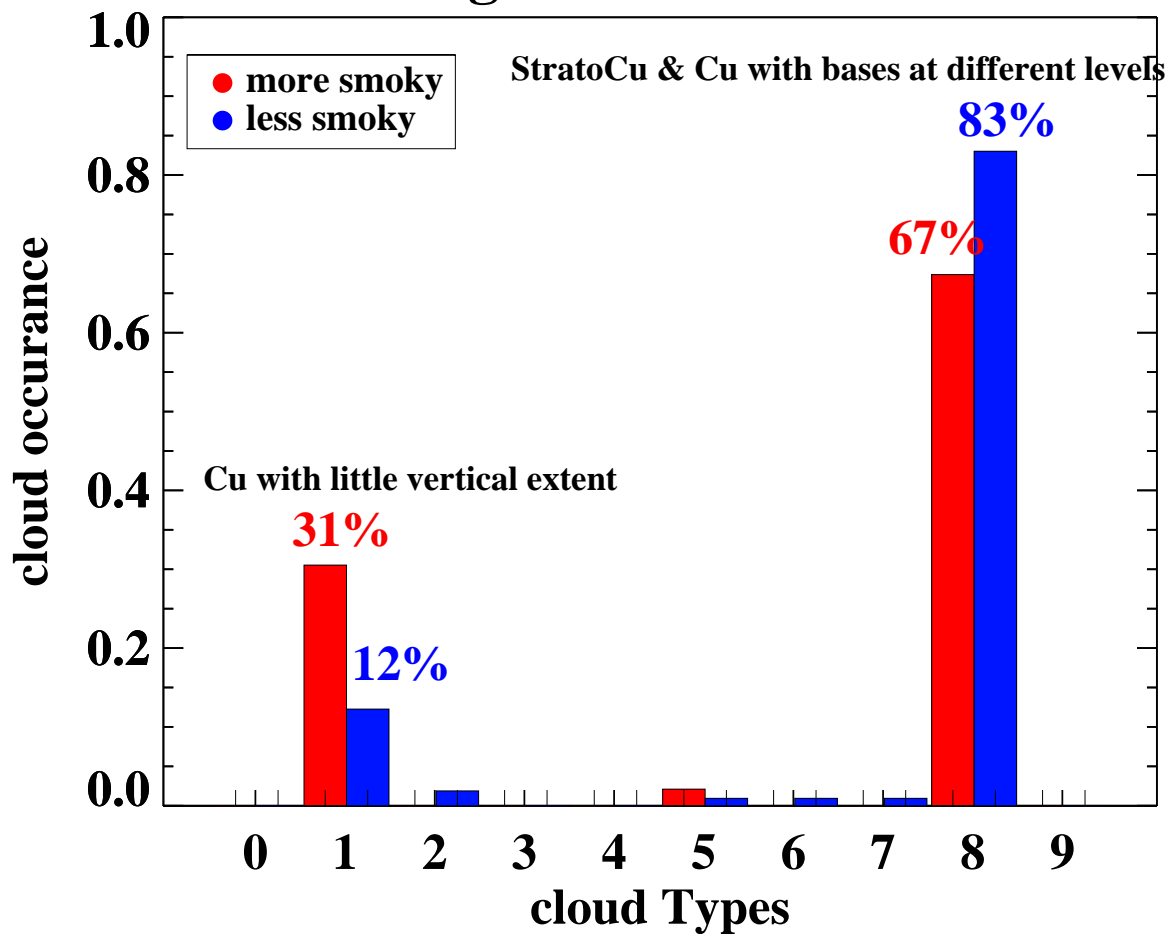
Figure 10. Frequency of occurrence of each WMO-defined surface-observed cloud type composited by "more" (red) and "less" (blue) smoky days.
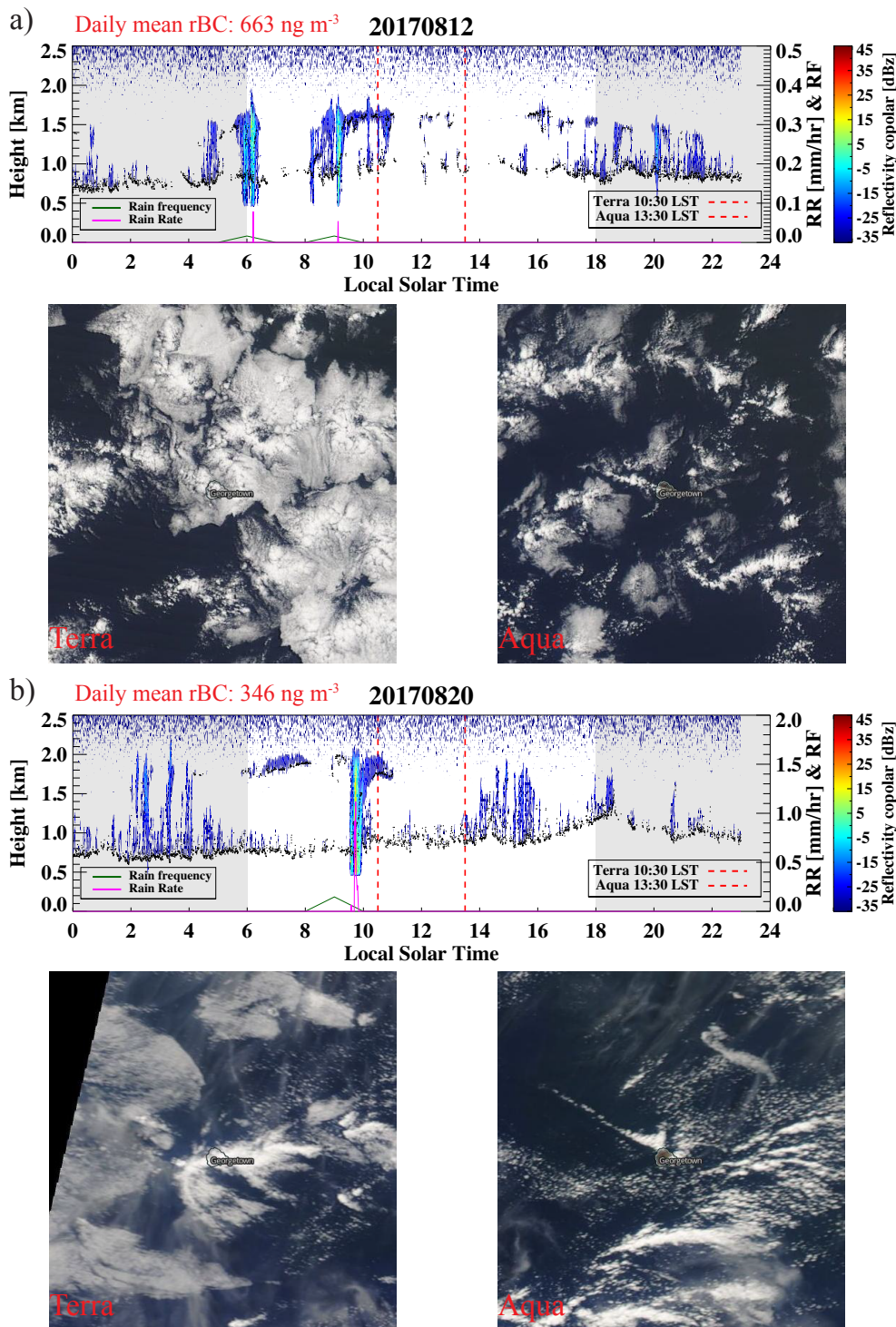
Figure 11. First and third rows: daily time series of the Ka-band zenith pointing cloud radar reflectivities (colored contour), disdrometer-derived one-minute rain rates (RR, magenta) and one-hour rain frequencies (RF, dark green), for a) August 12, 2017 and b) August 20, 2017. Ceilometer-detected cloud bases overlain in small black filled circles. Terra and Aqua overpass time indicated with red dashed lines. Second and fourth rows: corresponding 2° by 2° MODIS Terra and Aqua visible imagery centered on Ascension.
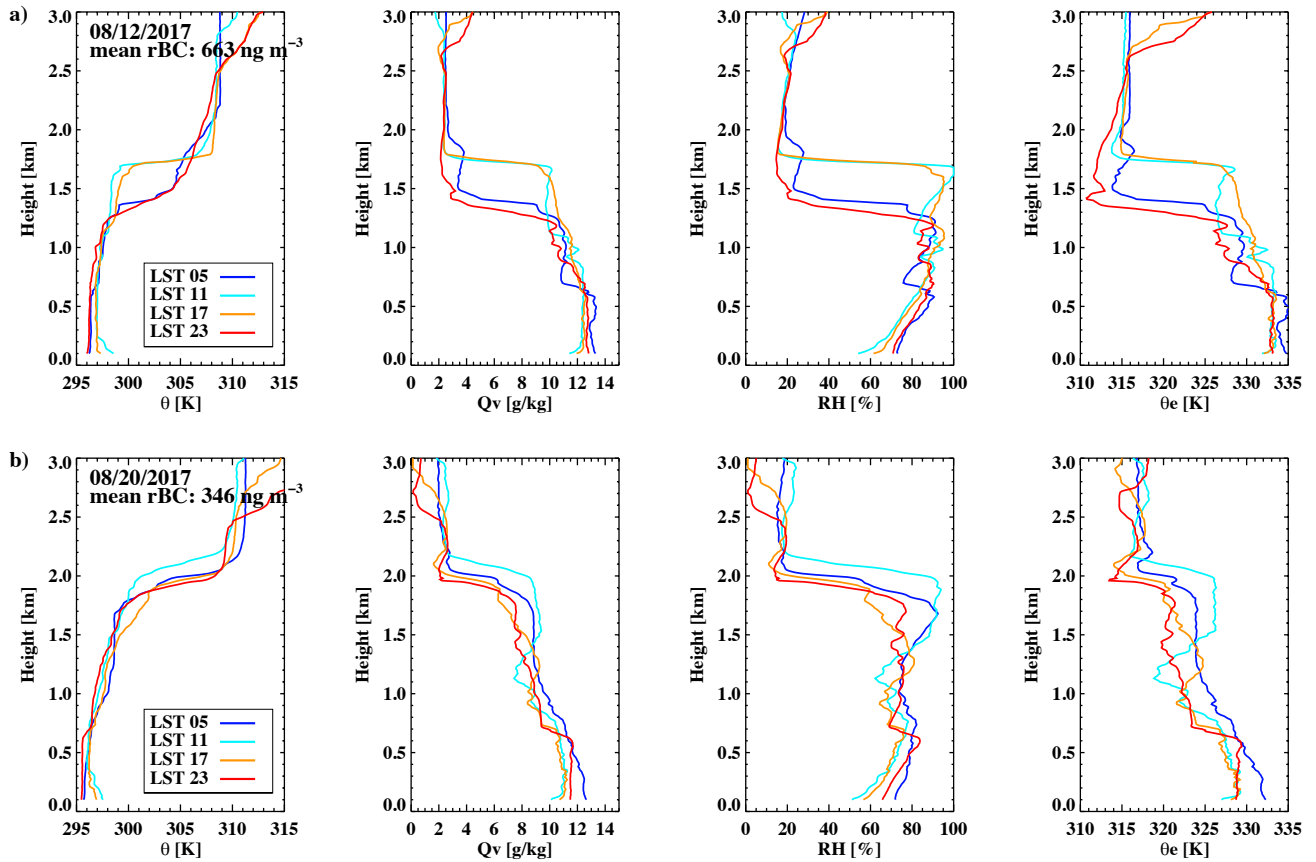
Figure 12. Individual radiosonde-derived profiles of (left to right) potential temperature, water vapor mixing ratio, relative humidity, and equivalent potential temperature for a) August 12, 2017 and b) August 20, 2017. Daily-mean black carbon mass concentration indicated on the left panel and radiosonde launch times within the legend.
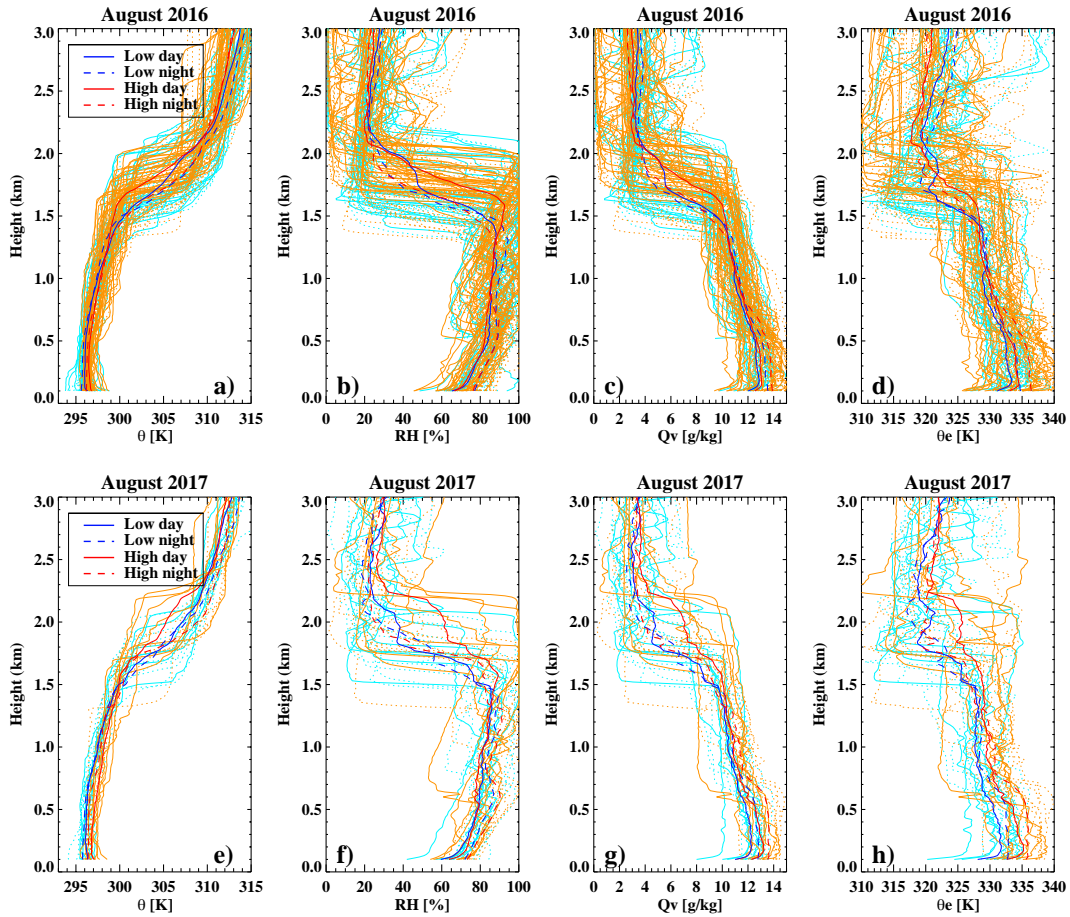
Figure 13. Radiosonde-derived vertical profiles of a) and e) potential temperature (θ), b) and f) relative humidity, c) and g) water vapor mixing ratio (Qv), and d) and h) equivalent potential temperature (θ_e) for August 2016 (upper) and 2017 (bottom), shown individually and as composite means (thicker solid lines for daytime, thicker dashed curves for nighttime) for "more" (red) and "less" (blue) smoke loadings. The smoke loadings are based on hourly-mean rBC values centered on the radiosonde launch time. 92 and 63 profiles contributed to the "more" and "less" smoke loading distribution, respectively, in 2016, and 29 and 27 profiles respectively in 2017.
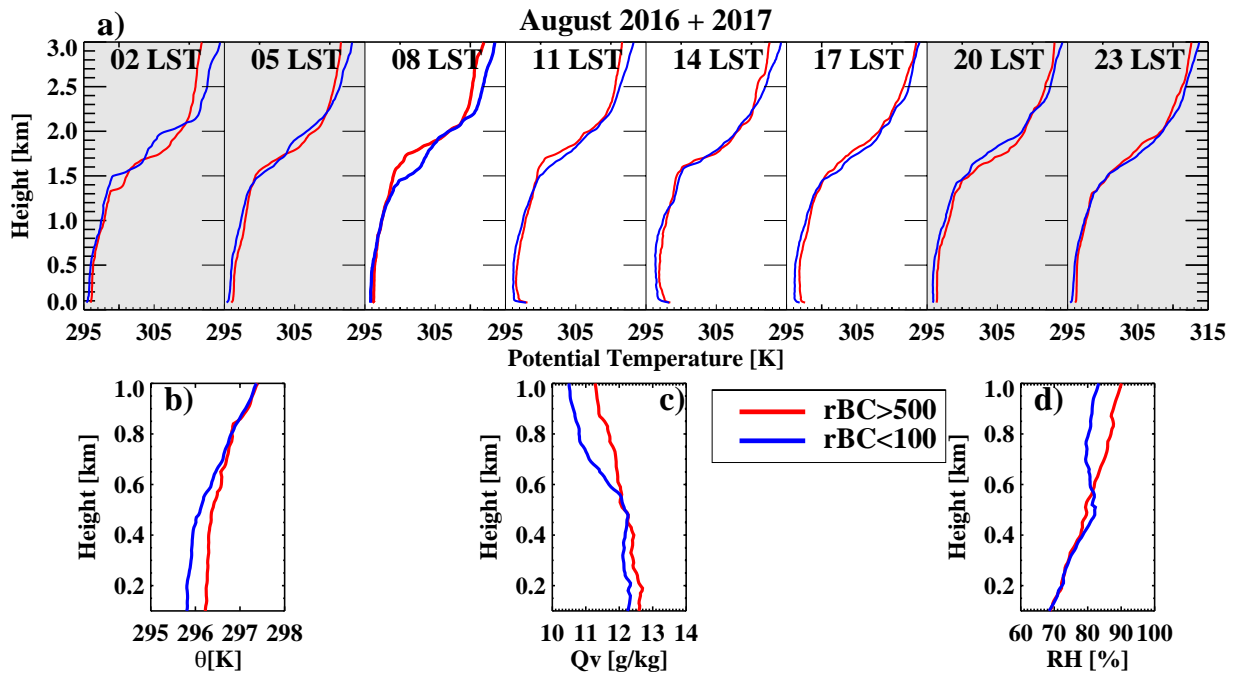
Figure 14. Three-hourly August-mean potential temperature profiles from a) 100 m to three km, and 8 LST 100 m to 1 km profiles for b) potential temperature (θ, c) water vapor mixing ratio (Qv), and d) relative humidity, composited for "more" (red) and "less" (blue) smoke loadings.
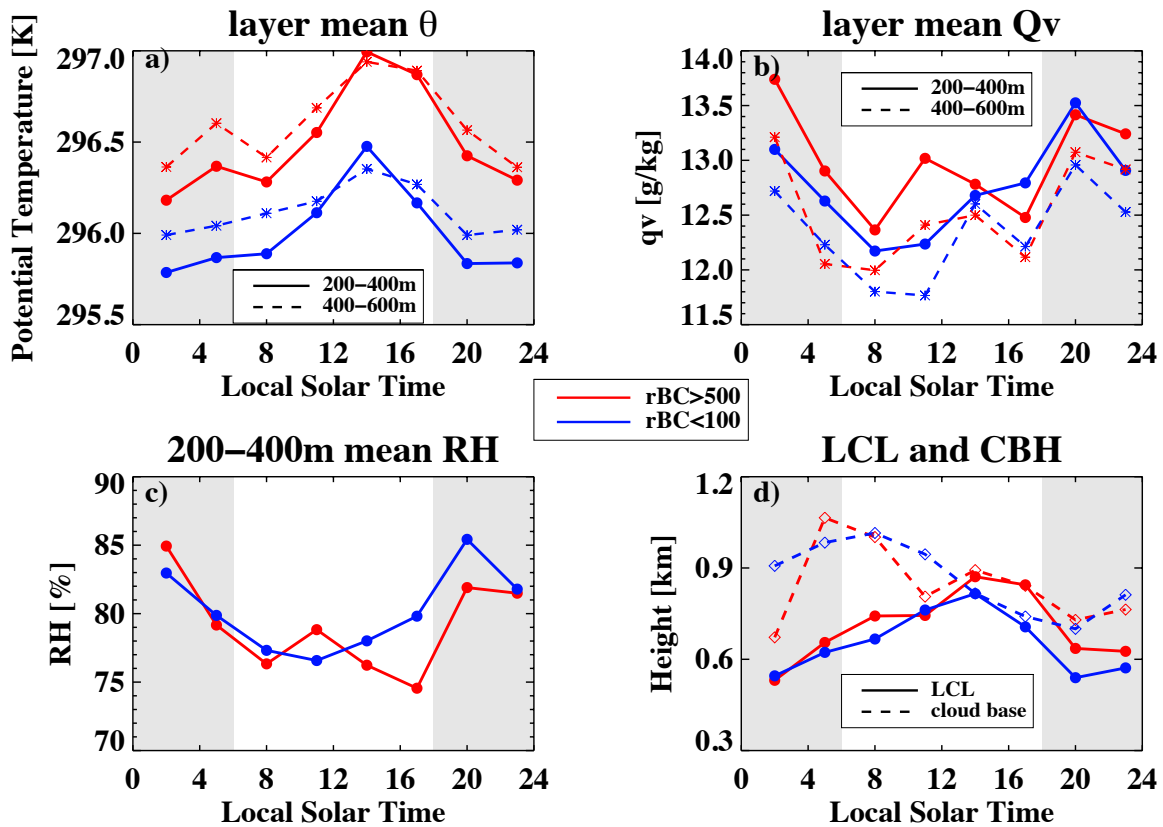
Figure 15. Diurnal cycle in the three-hourly radiosonde-derived 200-400 m (solid) and 400-600 m (dashed) layer-averaged a) potential temperature (θ), b) water vapor mixing ratio (Qv), and c) relative humidity (RH). d) Radiosonde-derived lifting condensation levels (LCLs) and the 10th percentile of the lowest ceilometer-derived cloud base. All are composited by days with "more" (red) and "less" (blue).
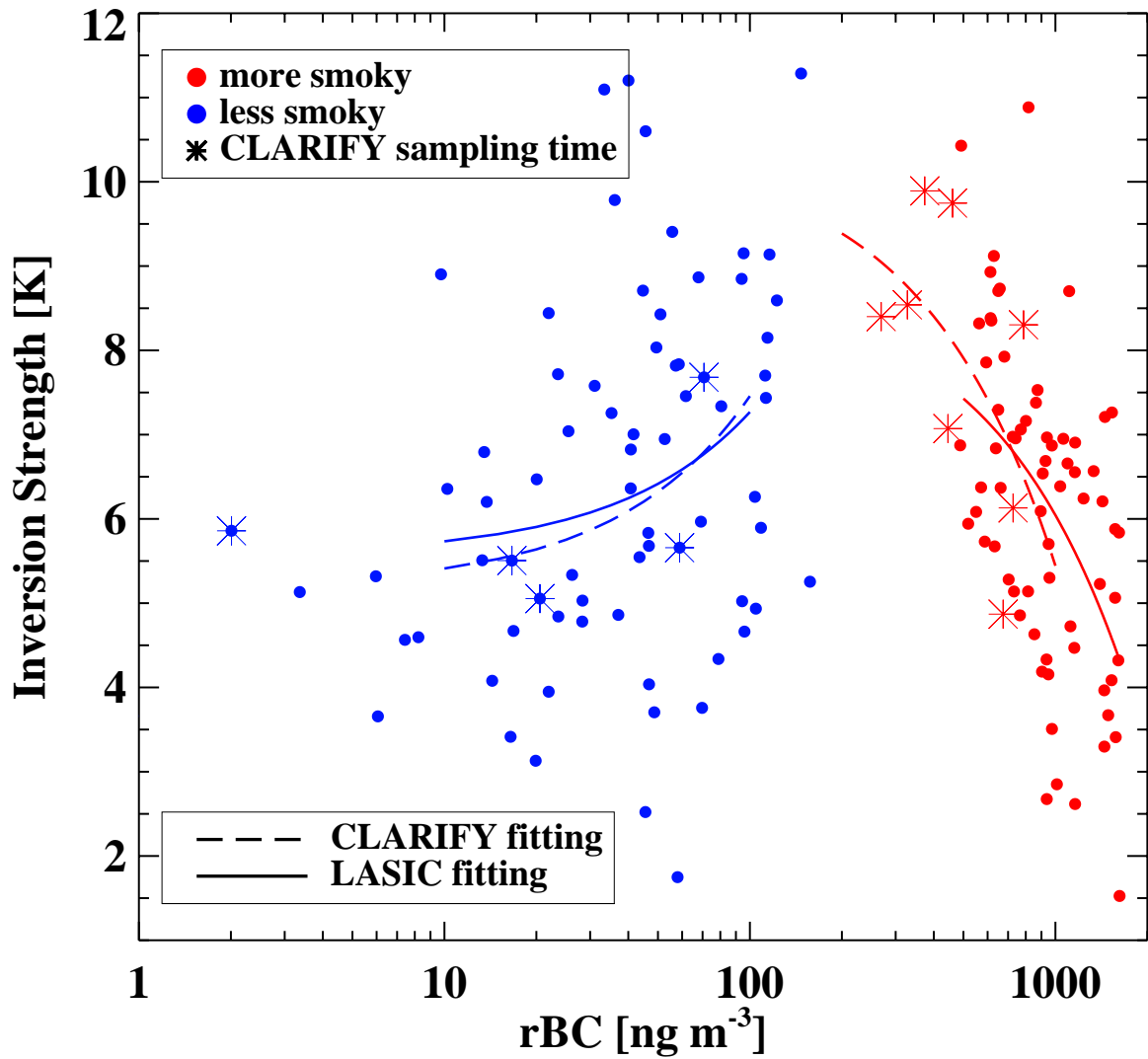
Figure 16. Radiosonde-derived inversion strength as a function of the refractory black carbon mass concentrations, with "more" (red) and "less" (blue) smoke loadings days indicated. Radiosonde-derived inversion strength values for the UK CLARIFY aircraft sampling periods are indicated as asterisks using the same color code. Linear fits are included for the two composites and the two campaigns. Note the logarithmic x-axis.
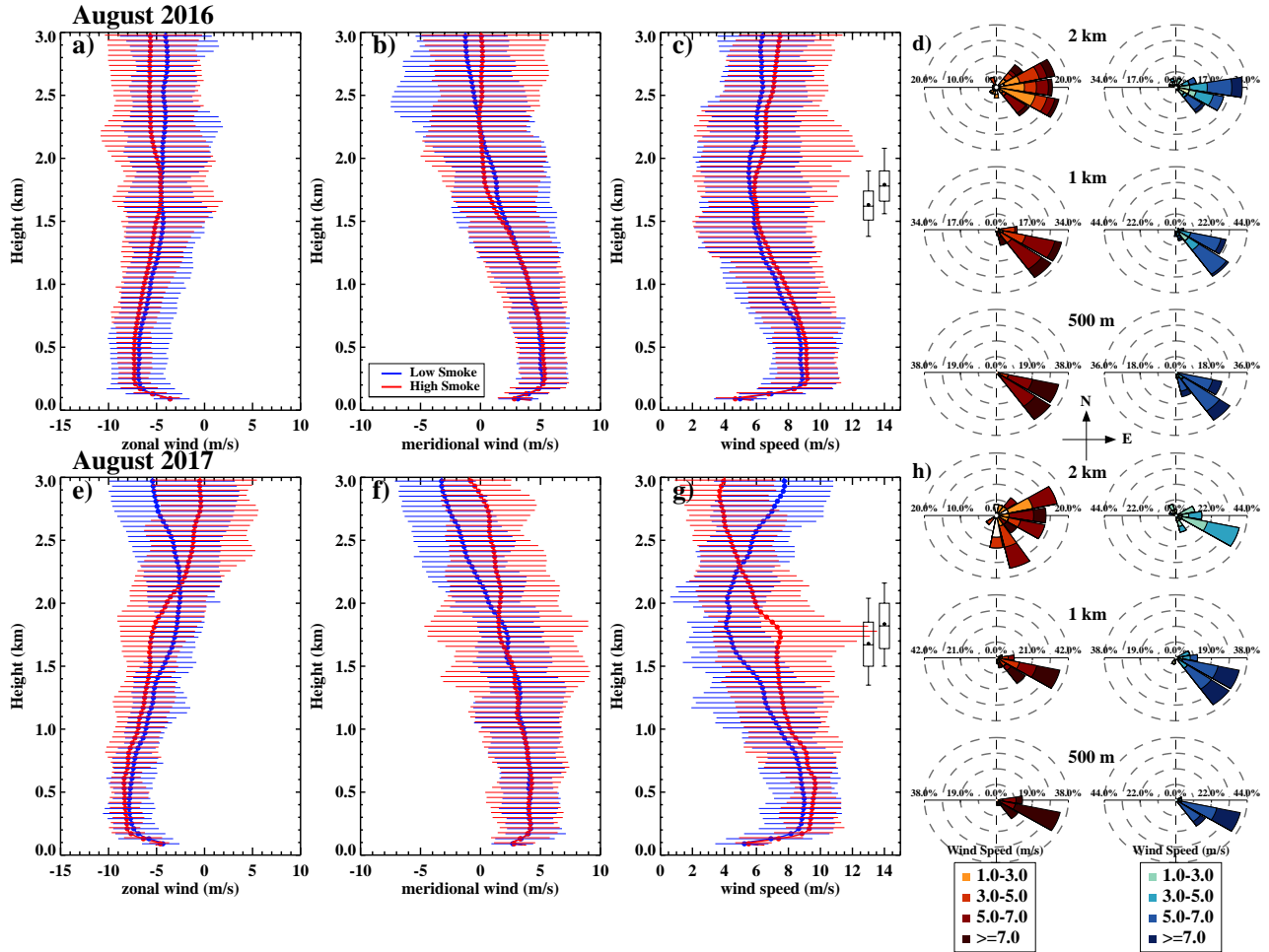
Figure 17. Radiosonde-derived a) and e) zonal wind profiles, b) and f) meridional wind profiles, and c) and g) mean wind speed profiles, for August 2016 (upper panel) and August 2017 (lower panel) for "more" (red) and "less" (blue) smoke loadings, respectively.. Solid thick curves indicate composite-mean, and horizontal bars indicate 10% and 90% percentiles. Inversion bases and tops indicated using mean values (black filled circles), and 10%, 25%, 75% and 90% percentiles (black box-whiskers) in c) and g). d) and f): Wind roses indicating wind directions at 500 m, one and two km for the two years, for days with "more" (left) and "less" (right) smoke.
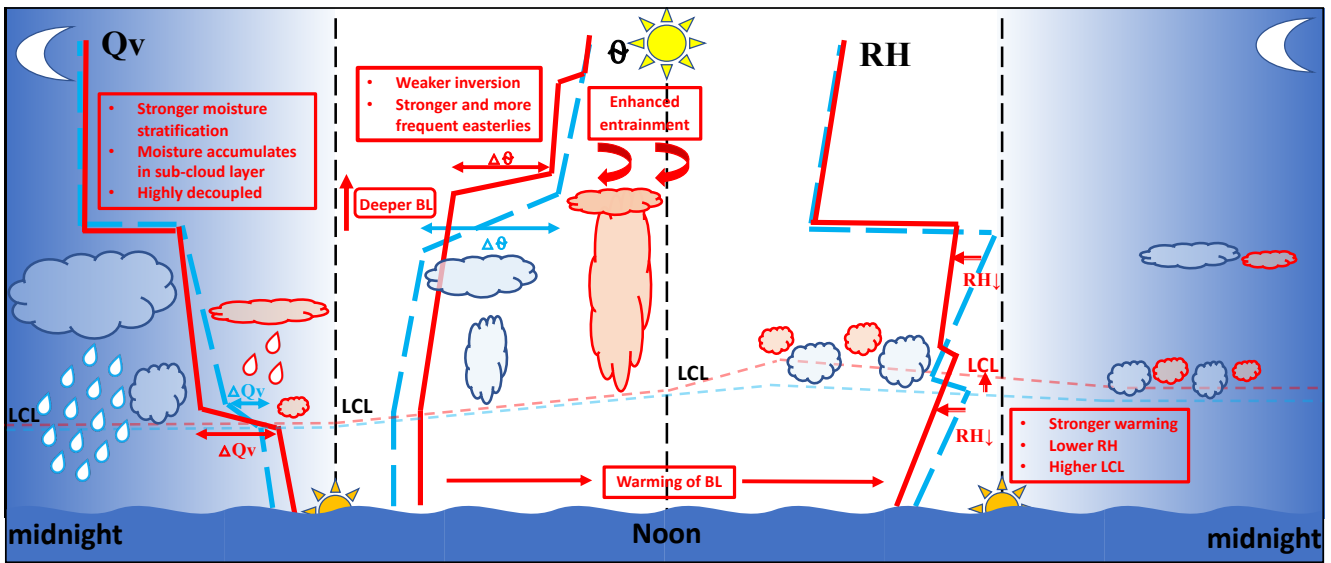
Figure 18. Schematic of the diurnal cycle for days with "less" (blue) and "more" (red) smoke, making use of the following abbreviations: Qv (water vapor mixing ratio), LCL (lifting condensation level), RH (relative humidity), $\Delta\Theta$ (change in potential temperature), and BL (boundary layer).

Table 1. Full list of datasets used in this paper with source/contact and remarks. The airport site is S1 and the AMF1 site is M1.

Name	Full Name	Uncertainties	contact	remarks
SONDE (S1)	Balloon-Borne Sounding System	0.5 °C and 5% RH	D. J. Holdridge, J. A. Prell, M. T. Ritsche, and R. Coulter	Vaisala, Inc. RS-92
CEIL (S1 and M1)	Vaisala Laser Ceilometer	cloud height measurement sensitivity: 10 m	V. Morris	Vaisala, Inc. CL31
SP2 (M1)	Single Particle Soot Photometer	3 ng m^{-3}	A. J. Sedlacek	Droplet Measurement Technologies, Inc.
CCN (M1)	Cloud Condensation Nuclei Particle Counter	activated particle sizing ±0.25 μm	G. Senum and J. Uin	Dual-chamber, values shown at 0.4% SS from Column A
MPL (M1)	Micropulse Lidar	see Delgadillo et al. (2018)	P. Muradyan	Sigma Space Corporation
DIS (M1)	Impact Disdrometer	range of diameter: 0.3 mm to 5 mm	M. J. Bartholomew	Distromet LTD Basel, Switzerland
SEVIRI	Spinning Enhanced Visible and Infrared Imager	N/A	NASA Larc	Visible Infrared Solar-Infrared Split Window Technique
CERES	Clouds and the Earth's Radiant Energy System	N/A	NASA Larc	Synoptic TOA and surface fluxes and clouds (SYN) products onboard Aqua and Terra
MODIS	Moderate Resolution Imaging Spectroradiometer	N/A	NASA	level-3 one-degree Onboard Terra and Aqua
CO (M1)	Carbon Monoxide Analyzer	±2 ppbv	S. Springston	Los Gatos Research
KAZR (M1)	Ka-band zenith pointing cloud radar	reflectivity copol ∼3 dBZ	N. Bharadwaj	-35 dBZ cutoff for clouds
SYNOP	UK Met Office SYNOP reports	N/A	CEDA Archive	Cloud type codes following WMO protocol
ERA5	Fifth generation of ECMWF atmospheric reanalyses of global climate	N/A	Copernicus Climate Change Service	Hourly 0.25° by 0.25°
MWR and MWRP (S1)	Microwave Radiometer (Profiler)	Tb ∼1 K LWP ∼0.015 mm	M. P. Cadeddu	MWRRET2 physical retrievals (23.8 GHz and 31.4 GHz)